5 Effects of the Hunga eruption on stratospheric ozone and related trace gases

Lead authors Freja F. Østerstrøm
Michelle L. Santee

Co-authors Martyn P. Chipperfield
Stéphanie Evan
Dan Smale
Krzysztof Wargan
David M. Wilmouth
Ingo Wohltmann

Contributing authors Ewa M. Bednarz
Sandip Dhomse
Eric L. Fleming
Stacey M. Frith
Gloria L. Manney
Luis F. Millán
Jun Zhang
Xin Zhou

Cite this as:

Østerstrøm, F. F., M. L. Santee et al. (2025): Effects of the Hunga eruption on stratospheric ozone and related trace gases. In APARC, 2025: The Hunga Eruption Atmospheric Impacts Report [Yunqian Zhu, Graham Mann, Paul A. Newman, William Randel (Eds.)]. APARC Report No. 11, WCRP Report No. 10/2025, DOI: [DOI-goes-here], available at `[project-website-or-landing-page]`.

Key points

This chapter presents the current state of knowledge of the immediate and longer-term effects of Hunga on global stratospheric composition. The extraordinary water vapour enhancement from the eruption triggered both heterogeneous and gas-phase chlorine activation, leading to rapid ozone loss in the fresh plume within one week. Over subsequent months, further heterogeneous chemical processing led to widespread perturbations in stratospheric chlorine and nitrogen partitioning of unprecedented magnitude and duration in the southern tropics and midlatitudes. Record-low abundances of stratospheric ozone were also seen at some altitudes in some regions; however, the degree of ozone destruction due to altered chemistry was minor, with ozone at low and middle latitudes being largely controlled by transport. Overall, Hunga did not strongly perturb total column ozone. The Hunga hydration was effectively excluded from the winter polar vortices in the first post-eruption winters in both hemispheres. While comparatively high humidity inside the 2023 Antarctic vortex prompted unusually early and vertically extensive chlorine activation and intensified dehydration, by mid-winter those processes had essentially run to completion, as is typical in the Antarctic, preventing an exceptionally severe springtime ozone hole. The Arctic vortex in the 2023/2024 winter/spring was also unusually moist, but dynamically disturbed conditions were unfavourable for chlorine-catalysed ozone loss. The effects on stratospheric composition from Hunga will diminish over the next decade as the excess water vapour is removed from the stratosphere through Antarctic dehydration and stratosphere-to-troposphere exchange.

The observed anomalous chemical processing following the eruption, on both short and longer-term timescales, resulted from well-known chemical reactions occurring on volcanic sulfate aerosol under conditions of highly enhanced stratospheric humidity unique in the observational record. No evidence of novel or previously unknown chemical mechanisms has been found.

Initial chemical processing and ozone loss in the fresh plume

- **The Hunga eruption triggered significant rapid ozone loss in the stratosphere over the tropical southwestern Pacific and Indian Ocean region, with ozone decreasing by 5% in less than two weeks.** The ozone loss was driven by the Hunga excess water vapour intensifying HO_x and ClO_x catalytic cycles, as well as heterogeneous chemistry on humidified volcanic aerosols; these mechanisms differ from those responsible for polar ozone loss. Although the eruption produced an unprecedented number of lightning flashes, lightning-generated NO_x was not a significant contributor to the initial in-plume ozone depletion. The extent to which similarly rapid ozone depletion may have occurred after previous major eruptions, such as El Chichón and Mount Pinatubo, is difficult to assess because comparable satellite and rapid-response observations were not available for those events. This highlights not only the exceptional nature of the Hunga eruption, but also the need for early-response campaigns and satellite instruments capable of monitoring stratospheric composition after major volcanic eruptions.

Longer-term impacts on stratospheric composition

Midlatitudes

- **Widespread changes in stratospheric composition of magnitude and duration unprecedented in the satellite record were observed at Southern Hemisphere (SH) midlatitudes in the months following the eruption.** In particular, perturbations in H_2O, HNO_3, HCl, ClO, and O_3 were seen.
- **The observed perturbations in trace gas distributions in the SH midlatitudes were brought about by altered chemistry and, more importantly in most cases, by altered transport.** The main heterogeneous reaction driving chemical changes was N_2O_5 hydrolysis, in contrast to the heterogeneous chlorine activation reactions that lead to lower stratospheric polar ozone destruction. Ozone-loss cycles involving HO_x and ClO_x were enhanced, while NO_x-driven ozone loss slowed. However, although heterogeneous chemistry also played a role, as evidenced by correlations with the transport tracer N_2O as well as atmospheric modelling, changes in stratospheric circulation (possibly linked to Hunga) were primarily responsible for the observed anomalies in HCl, HNO_3, and O_3.

Tropics

- **Satellite observations reveal substantial post-eruption perturbations in the composition of the tropical stratosphere. Model simulations show that these perturbations arise from heterogeneous chemical processing on volcanic sulfate aerosol.** Impacts are seen in the tropics several months before they become evident at midlatitudes, consistent with the evolution of the Hunga water vapour and aerosol. N_2O_5 hydrolysis is identified as the main mechanism driving chlorine and nitrogen repartitioning.
- **Although the ClO enhancements observed in the tropics in 2022 were exceptional for that latitude band, they were still more than an order of magnitude weaker than those seen during a typical polar winter/spring in either hemisphere.** The evolution of ozone abundances in the tropical stratosphere in 2022, while affected by anomalous chemistry to some degree, was dominated by transport. The extent to which transport anomalies in the tropics were causally connected to the eruption is not clear.

Antarctic winters/springs of 2022, 2023, and 2024

- **The Hunga water vapour was effectively excluded from the 2022 Antarctic polar vortex by the strong transport barrier at the vortex edge, and consequently the heterogeneous chemical processing and ozone loss that took place within it were near average.** After the vortex broke down in November–December 2022, enhanced stratospheric water vapour and aerosols pervaded the southern high latitudes.
- **Although Hunga enhanced polar stratospheric cloud (PSC) formation and chlorine activation early in the 2023 season, by July/August lower stratospheric abundances of HCl, ClO, HNO_3, and H_2O had returned to their respective climatological mean values. Thus chlorine activation, denitrification, and dehydration processes had saturated by mid-winter, as is typical in the Antarctic, preventing an exceptionally severe ozone hole in 2023.** The extraordinary moisture from Hunga prompted unusually early and vertically extensive PSCs, and dehydration subsequently removed ~50% more water vapour than typical. Heterogeneous chlorine activation also occurred weeks earlier and at higher altitudes than previously observed, but the early-winter upper-level activation was too weak to cause substantial ozone loss. For the most part, observational and modelling studies found only a minor effect on the 2023 Antarctic ozone hole, with the additional Hunga-induced ozone loss (which largely occurred in the region along the vortex edge where chlorine is typically not fully activated) being within the observed year-to-year variability.
- **As a result of unusually strong planetary wave activity, the Antarctic vortex was relatively warm through much of the 2024 season; although conditions inside the vortex were again moister than usual, lower stratospheric chemical processing mostly followed typical patterns, and ozone abundances were near or slightly above average.**

Arctic winters/springs of 2021/2022, 2022/2023, and 2023/2024

- **Hunga hydration has so far had minimal impact on chemical processing and ozone loss in the Arctic winter polar vortex.** The Hunga water vapour had not yet reached the northern polar latitudes by boreal spring 2022, while in spring 2023 it was not able to penetrate the Arctic vortex. Although extraordinarily high water vapour abundances were present inside the 2023/2024 Arctic vortex, comparatively warm and dynamically disturbed conditions during that winter/spring were unfavourable for substantial chemical ozone loss.

Predictions of the future impacts on the stratospheric ozone layer

- **Observations and model simulations indicate that the Hunga hydration will persist through the end of this decade.** MLS measurements and model simulations identify dehydration through sedimentation of ice PSCs in Antarctic winter as the primary removal pathway for the excess Hunga water vapour at work initially. Stratosphere-to-troposphere transport (STT) at middle and high latitudes

as part of the meridional Brewer–Dobson circulation began to play a major role after the Hunga-hydrated air parcels had descended to sufficiently low altitudes in late 2023. Once removal processes commenced, the e-folding decay time estimated from both measurements and models is 2.5–4 years, leading to a lifetime (i.e., mean stratospheric residence time) of 4–5.5 years.

- **Minor effects on ozone, in most cases indistinguishable against the backdrop of interannual variability, can be expected to continue until the excess Hunga water vapour has been removed from the stratosphere.** Model studies indicate that the largest Hunga impacts on column ozone occur in the polar regions, in particular the Antarctic.

Contents

Preamble

Chapter 5 presents and assesses the current understanding of the immediate and longer-term impacts on stratospheric composition of the eruption of the Hunga volcano (see Chapter 1 for details of the eruption). Observational and modelling studies that have examined the effects of Hunga on composition at low, middle, and high latitudes throughout the stratosphere are concisely summarised. The chapter also describes projections of the Hunga water vapour evolution and how its effects on stratospheric composition are expected to diminish over the next decade.

Observations of stratospheric chemical composition, aerosol, and clouds reported here come mainly from satellite-borne sensors: the Aura Microwave Limb Sounder (MLS), the SCISAT Atmospheric Chemistry Experiment-Fourier Transform Spectrometer (ACE-FTS), the Suomi-NPP Ozone Mapping and Profiler Suite Limb Profiler (OMPS-LP) and Nadir Profiler (OMPS-NP), the Solar Backscatter Ultraviolet (SBUV, SBUV/2) series of instruments, and the Cloud-Aerosol Lidar and Infrared Pathfinder Satellite Observations (CALIPSO) Cloud-Aerosol Lidar with Orthogonal Polarization (CALIOP). High-resolution profiles of ozone and water vapour from balloon-borne sondes are also used. An overview of observational platforms that sampled the compositional changes following the Hunga eruption, including descriptions of observational techniques, data coverage, and measurement quality, can be found in Supplementary S2 of this report.

Intermodel and model-to-measurement comparisons of the impact of the Hunga eruption are being undertaken as part of the Hunga Tonga–Hunga Ha'apai Model Observations Comparison (HTHH-MOC) and Hunga Tonga–Hunga Ha'apai Volcano Model Intercomparison Project (Tonga-MIP). The specifics of the model experiment protocol and descriptions of the different chemical transport models (CTMs) and chemistry–climate models (CCMs) participating in these efforts are given in Supplementary S1 for HTHH-MOC and Supplementary S5 for Tonga-MIP. In addition to those included here, other HTHH-MOC results relevant to the chapter are shown in Supplementary S3. Chapter 5 also discusses simulations from models that are not part of those intercomparisons; descriptions of these models are provided in Supplementary S4.

5.1 Overview of Hunga effects on total column ozone

To set the stage for subsequent discussion, Figure 5.1 shows the long-term (1979–2025) record of anomalies (i.e., deviations from climatological values) in total column ozone. While a substantial reduction in total column ozone is seen in much of the Southern Hemisphere (SH) in 2022, negative (and positive) anomalies of comparable or greater magnitude have occurred throughout the observational record, and the post-Hunga changes do not stand out in the context of the considerable interannual variability in total column ozone. Hunga-induced anomalies in ozone and related trace gases are more striking at some altitudes in some regions, as discussed in detail in the following sections.

5.2 Initial chemical processing and ozone loss in the fresh plume

The eruption of the Hunga volcano on 15 January 2022 offered a unique opportunity to investigate the early impacts of a tropical eruption on stratospheric composition. A balloon campaign was set up within a week at the Maïdo Observatory, Réunion Island (21°S, 55°E). From 20 to 24 January 2022, meteorological balloons carrying aerosol, water vapour (H_2O), sulfur dioxide (SO_2), and ozone (O_3) instruments measured the plume's composition. These and other observations revealed the unprecedented stratospheric injection of water vapour (see Chapter 2). This rapid-response campaign provided a rare dataset for studying early chemical processes in a fresh volcanic plume.

Significant stratospheric composition changes following the Hunga eruption were reported based on a combination of satellite data from Aura MLS and balloon-borne as well as ground-based measurements (Evan et al., 2023). The night of 22 January 2022, when the Cryogenic Frostpoint Hygrometer instrument at Maïdo Observatory recorded the highest post-eruption stratospheric water vapour mixing ratio (350 ppmv at 26.5 km), also corresponded to the largest ozone decreases observed in the balloon profiles (10–45%, relative to the 1998–2021 climatology; Figure 5.2a). This specific case helped define the H_2O threshold of 100 ppmv used to extract MLS anomalies of O_3, HCl, and ClO shown in Figure 5.2b, ensuring that these anomalies represent Hunga plume conditions. Balloon-borne and MLS observations near 20°S indicated an average ozone anomaly of −0.5 ppmv and −0.4 ppmv, respectively, within the altitude range 25–29 km (corresponding to approximately 14–25 hPa

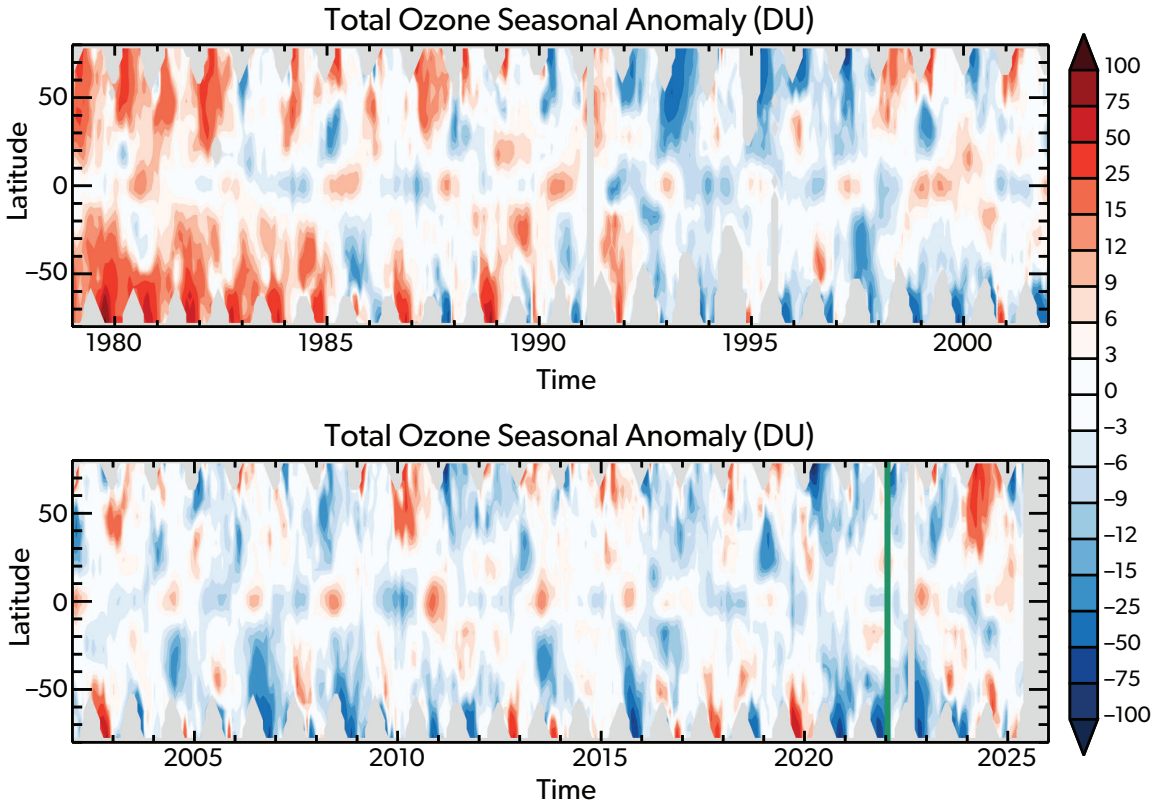

Figure 5.1: *Total column ozone seasonal anomalies (in Dobson Units, DU), plotted as a function of time (1979 to mid-2025) and latitude (80°S to 80°N). Total ozone anomalies were computed from the version 8.7 SBUV Merged Ozone Data (SBUV MOD) record (Frith et al., 2014; Frith et al., 2017; Godin-Beekmann et al., 2022). SBUV MOD is a combined record of total and profile ozone measurements from the SBUV, SBUV/2, and OMPS-NP instrument series. Seasonal anomalies were computed by subtracting the 1979–2025 seasonal climatology. Grey shading marks regions of missing data, and the vertical green line marks the date of the Hunga eruption.*

or 620–770 K) over the period 16–24 January (Figure 5.2b). The 0.4 ppmv decrease in ozone observed over 25–29 km exceeds ±1 standard deviation of the MLS ozone climatology, indicating that it lies outside the typical range of variability (not shown). This decline corresponds to an approximate 5% reduction in ozone at these altitudes. Additionally, MLS observations indicated a 0.25 ppbv decrease in hydrochloric acid (HCl, the main reservoir for chlorine in the stratosphere), corresponding to an approximate 20% reduction over the same altitude range (Figure 5.2b). In parallel, chlorine monoxide (ClO, the primary form of ozone-destroying reactive chlorine) increased by 0.37 ppbv (Figure 5.2b).

Heterogeneous chlorine activation on humidified volcanic aerosols was found to play a major role in facilitating the observed rapid ozone depletion (Evan et al., 2023). These processes were further explored using 3-D CCM simulations from the Whole Atmosphere Community Climate Model version 6 (WACCM6) to distinguish the chemical and dynamical drivers of the initial in-plume ozone reduction (Zhu et al., 2023). The model simulations tested various injection scenarios involving H_2O, SO_2, HCl, and ClO to assess their respective impacts on ozone depletion. There is no observational evidence for a direct injection of ClO into the stratosphere by the Hunga eruption, and although MLS did measure elevated HCl abundances in a handful of profiles immediately following the eruption (Millán et al., 2022; Santee et al., 2023), the relatively modest HCl injection from Hunga is unlikely to have had a major impact on available chlorine in the plume. Nevertheless, both of these scenarios were tested in the model to investigate the effects of the presence of additional reactive chlorine, and the ClO injection case yielded results equivalent to those obtained when injecting HCl.

The simulations highlighted the key role of the H_2O injection in amplifying chlorine activation and ozone depletion through enhanced heterogeneous and gas-phase chemical processes. Figure 5.2c shows that the average simulated ozone anomaly is −0.22 ppmv at

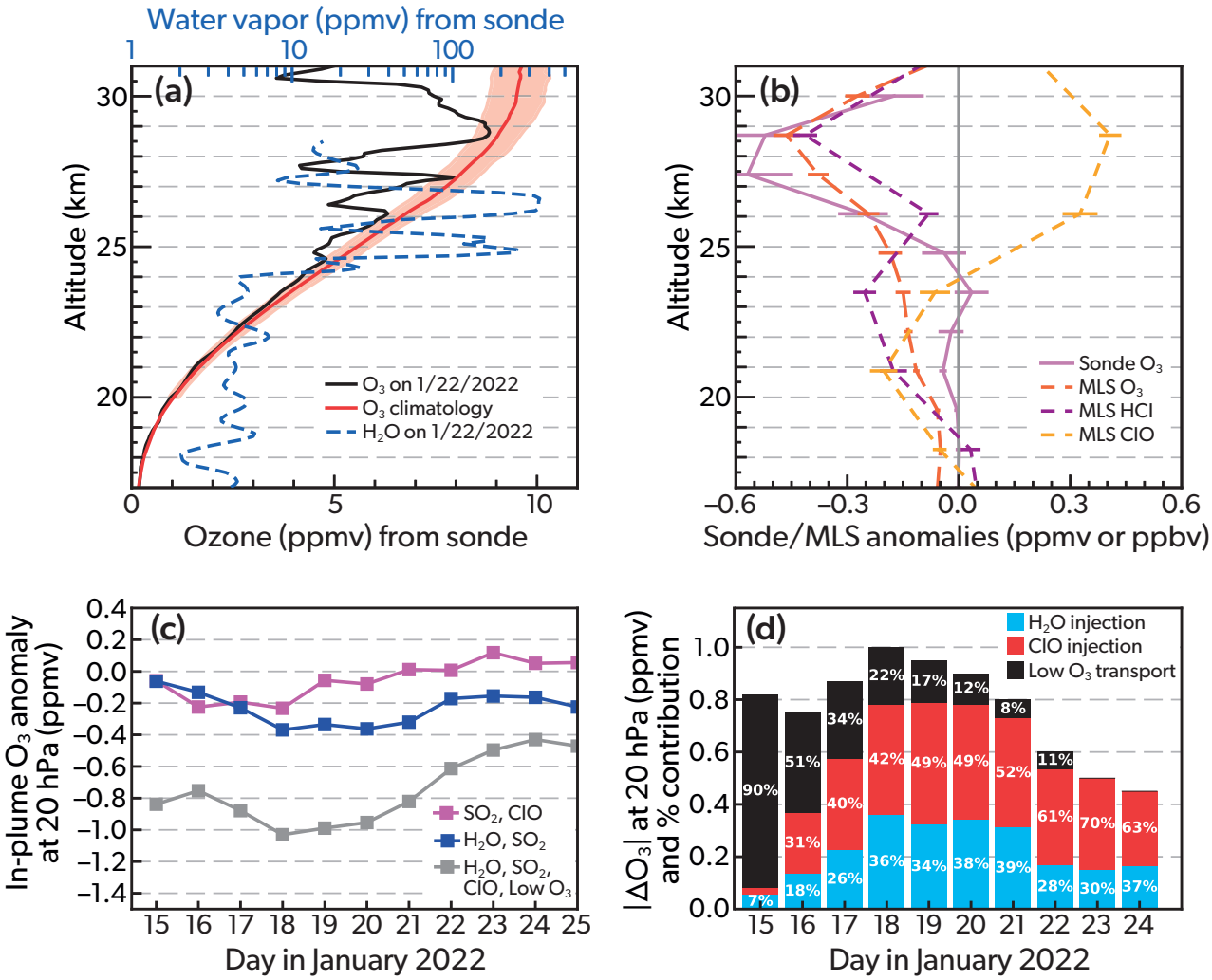

Figure 5.2: *(a) Ozone and water vapour soundings at Maïdo Observatory on 22 January 2022, the night of the highest water vapour mixing ratio recorded by the Cryogenic Frostpoint Hygrometer (dashed blue line). The solid black line shows the ozone mixing ratio measured at Maïdo on 22 January, exhibiting multiple ozone loss layers compared to the Réunion climatology (1998–2021, solid red line). Red shading indicates ±1 standard deviation of the Réunion climatology. (b) Ozonesonde-derived mean anomalies for O_3 (solid magenta line), as well as MLS-derived mean anomalies for O_3 (dashed red line), HCl (dashed purple line), and ClO (dashed orange line), averaged over 16–24 January. MLS anomaly profiles were computed using an H_2O threshold of 100 ppmv to ensure that they represent Hunga plume conditions. Error bars on each anomaly profile represent the standard error of the mean anomaly. (c) Daily average simulated in-plume ozone anomaly at 20 hPa from WACCM6 model runs. Different model scenarios are represented: H_2O and SO_2 co-injection (blue); SO_2 and ClO co-injection (magenta); and H_2O, SO_2, and ClO co-injection with transport of ozone-poor air from the troposphere (grey). (d) Percentage contributions to the absolute values of daily mean ozone anomaly ($|\Delta O_3|$) at 20 hPa in WACCM6 simulations from H_2O injection (blue), ClO injection (red), and low-O_3 air transported from the troposphere (black). Contributions were estimated by incrementally adding each process: the H_2O contribution reflects the ozone loss from comparing the H_2O/SO_2 injection scenario to the no-volcano baseline; the ClO contribution compares the H_2O/SO_2/ClO scenario to the H_2O/SO_2 case; and the low-O_3 contribution compares the H_2O/SO_2/ClO/LowO_3 scenario to the H_2O/SO_2/ClO scenario (Zhu et al., 2023). While no observational evidence exists for direct ClO injection by the Hunga eruption, this scenario was tested in the model and produced results equivalent to those obtained assuming HCl injection. Thus, results for the "ClO injection" scenario are shown in (c) and (d). Data from Evan et al. (2023).*

20 hPa (~27 km) over 15–25 January for the "H_2O, SO_2" scenario, reflecting ozone depletion driven by Hunga H_2O-enhanced activation of background chlorine (either via gas-phase chemical processes or via heterogeneous chemistry subsequent to the formation of sulfate aerosols). This is smaller than the observed anomalies of −0.5 ppmv and −0.4 ppmv measured by ozonesondes and MLS, respectively, within the 25–29 km altitude range (Figure 5.2b). Notably, in the "SO_2, ClO" scenario, in which no H_2O is injected, the average simulated ozone anomaly is only −0.05 ppmv, indicating that ClO alone, without the presence of enhanced water vapour, results in minimal ozone depletion.

In the "H_2O, SO_2, ClO, low-O_3" scenario, the simulated ozone anomalies deepen to −0.75 ppmv over the same period, with two additional processes contributing to this enhanced depletion. During the first few days (15–16 January), the injection of ozone-poor air from the troposphere dominates, accounting for more than 50% of the ozone loss at 20 hPa (Figure 5.2d). However, this contribution declines rapidly and becomes minor (<10%) by 21 January. After this date, the enhanced ozone loss is primarily driven by elevated ClO levels, introduced in the model as a sensitivity test to isolate the effect of additional reactive chlorine, analogous to what might result if HCl were injected and subsequently activated, as discussed by Zhu et al. (2023).

The somewhat larger simulated ozone anomalies in the WACCM6 "H_2O, SO_2, ClO, low-O_3" scenario, particularly during the early simulation period (15–21 January; Figure 5.2c), likely stem from challenges in representing the initial dispersion of the highly humidified plume with WACCM6's relatively coarse vertical and horizontal resolution, as well as uncertainties in modelling rapid chlorine activation processes and the transport and mixing of ozone-poor air from the troposphere. However, when considering the mean simulated ozone decrease for the later period (22–25 January), when the transport and mixing of low-O_3 air from the troposphere had stabilised, the simulated average ozone decrease for the "H_2O, SO_2, ClO, low-O_3" scenario is −0.5 ppmv (Figure 5.2c). This value agrees well with the mean O_3 anomaly derived from measurements in Figure 5.2b.

The massive injection of water vapour led to a substantial rise in hydroxyl radical (OH) production rates (Zhu et al., 2022; Zhu et al., 2023; Fleming et al., 2024). Elevated OH abundances played a critical role in accelerating ozone depletion by participating in catalytic cycles that convert ozone into molecular oxygen (O_2). The increased H_2O levels enhanced the hydrogen oxide (HO_x = OH + HO_2) catalytic cycles, which consist of OH and hydroperoxyl (HO_2) radicals in various reactions with ozone and oxygen atoms. Specifically, the rates of key reactions increased by a factor of four. This heightened activity of OH and HO_2 radicals not only contributed to the rapid ozone loss observed, but also facilitated interactions with chlorine compounds, further driving the depletion of ozone through HO_x–chlorine oxide (ClO_x = Cl + ClO + 2 × ClOOCl) cycles. These chemical processes were largely confined within the layer around ~20 hPa, where the highest H_2O mixing ratios were observed. At this altitude, the extreme water vapour injection significantly enhanced chlorine activation, amplifying catalytic ozone loss (Zhu et al., 2023). Overall, the model results (Figures 5.2c–5.2d) indicated that the primary drivers of the observed reduction in ozone were threefold: increased H_2O injection enhanced the HO_x catalytic cycle and its interaction with the ClO_x catalytic cycle; enhanced ClO abundances, which arose through both heterogeneous and gas-phase reactions, induced ozone loss; and the rising volcanic plume introduced ozone-poor tropospheric air into the stratosphere.

Additionally, a large enhancement in HOCl and its photolysis rate within the plume were found to play a critical role in gas-phase chlorine repartitioning (Zhu et al., 2023). Moreover, the rate of the heterogeneous reaction (see Reaction R5.1 in Box 5.1) between HOCl and HCl, forming molecular chlorine (Cl_2) and H_2O, increased by 10 orders of magnitude, making it a major driver of chlorine activation. This distinguishes the chlorine activation mechanism in the fresh Hunga plume from that in the winter polar lower stratospheric vortices, where Reaction R5.2 between HCl and chlorine nitrate ($ClONO_2$) plays a dominant role.

The Hunga eruption also generated significant lightning activity (e.g., Van Eaton et al., 2023), leading to potential production of nitrogen oxides (NO_x = NO + NO_2). Thus, the impact of lightning-generated NO_x within the Hunga volcanic plume was also explored (Zhu et al., 2023). The simulations, which included an injection of 0.003 Tg of nitrogen monoxide (NO), inferred from the number of lightning flashes detected after the eruption, indicated that the additional NO_x had little effect on ozone loss in the first 10 days after the eruption. This is likely because the high water vapour content in the plume rapidly converted NO to nitric acid (HNO_3), limiting its influence

on ozone depletion. Satellite observations from MLS did not indicate a significant enhancement of HNO_3 in the initial volcanic plume in January 2022 (Millán et al., 2022; Santee et al., 2023). The measured HNO_3 remained within the range of typical variability, suggesting that the total NO production was insufficient to cause a noticeable increase in HNO_3. Therefore, lightning-generated NO_x was not considered a significant contributor to the initial in-plume ozone depletion observed immediately following the Hunga eruption.

In summary, the rapid (within one week) ozone loss observed in the Hunga plume resulted from well-known chemical reactions occurring under the highly unusual atmospheric conditions triggered by the eruption. While sulfate aerosols typically promote heterogeneous chemistry after major eruptions, in this case, the exceptional water vapour injection (which far exceeded typical variability) played a critical role in enhancing chlorine activation and ozone loss.

The ~5% ozone loss in the Hunga plume immediately following the eruption appears to stand out in the observational record of stratospheric ozone changes after major volcanic eruptions, such as El Chichón in 1982 and Mount Pinatubo in 1991. However, no comparable rapid-response campaigns were conducted after those eruptions, nor were they initially observed with satellite instruments capable of providing detailed stratospheric composition measurements like MLS. As a result, it is difficult to determine whether similarly rapid tropical ozone depletion occurred immediately following previous major eruptions but went unobserved due to limited measurements. This highlights both the exceptional nature of the Hunga eruption and the importance of rapid-response observations for fully capturing the immediate atmospheric impacts of major volcanic eruptions.

5.3 Longer-term impacts on stratospheric composition

5.3.1 Midlatitudes

Following the initial early impacts of the Hunga eruption (Section 5.2), significant and prolonged changes in stratospheric composition were observed at SH midlatitudes (Santee et al., 2023; Wilmouth et al., 2023). MLS measurements taken in 2022 show anomalies of unprecedented magnitude and duration in H_2O, ClO, HNO_3, HCl, and O_3 relative to previous years in the data record, which began in 2004. Other instruments similarly observed substantial perturbations to stratospheric composition at SH midlatitudes. These changes were caused by both altered transport and altered chemistry following the stratospheric injection of H_2O and SO_2 (Santee et al., 2023; Wilmouth

Box 5.1. Heterogeneous reactions important to stratospheric ozone

Heterogeneous reactions involve interactions between gas-phase molecules and aerosols in the stratosphere and play an important role in stratospheric ozone chemistry. Aerosols can have many different compositions, but the most common form is an aqueous suspension of sulfuric acid (Junge et al., 1961). At the extremely low temperatures typical of the stratospheric polar regions in wintertime, polar stratospheric clouds (PSCs) can form. PSCs vary in composition but most commonly consist of hydrated droplets of nitric acid and sulfuric acid (Tritscher et al., 2021). PSCs provide surfaces for heterogeneous reactions to take place that drive large seasonal ozone losses in the polar regions in both hemispheres in winter and spring. Important heterogeneous reactions on aerosol surfaces relevant to ozone in the stratosphere include (e.g., Solomon, 1999 and references therein):

$$HCl + HOCl \rightarrow Cl_2 + H_2O \quad (R5.1)$$
$$HCl + ClONO_2 \rightarrow Cl_2 + HNO_3 \quad (R5.2)$$
$$ClONO_2 + H_2O \rightarrow HOCl + HNO_3 \quad (R5.3)$$
$$N_2O_5 + H_2O \rightarrow 2 \times HNO_3 \quad (R5.4)$$
$$BrONO_2 + H_2O \rightarrow HOBr + HNO_3 \quad (R5.5)$$
$$HOBr + HCl \rightarrow BrCl + H_2O \quad (R5.6)$$

These reactions serve to both (1) shift chlorine and bromine from reservoir forms to more active forms that can be readily photolyzed to release Cl and Br and thus destroy ozone, and (2) shift nitrogen into the longer-lived reservoir form of HNO_3. The heterogeneous reaction rates involving chlorine (all but R5.4 and R5.5) are extremely temperature dependent. All of the reactions listed become enhanced (although not necessarily to the point of stratospheric significance) when sulfate surface area density is elevated, such as following a volcanic eruption.

et al., 2023; Zhang et al., 2024a; Bednarz et al., 2025).

Satellite observations for aerosol and a number of chemical constituents following the eruption, along with previous years of data for climatological context, are shown in Figure 5.3. Data have been averaged over a range of SH midlatitudes, 38°S–54°S equivalent latitude (EqL, a Lagrangian coordinate calculated from potential vorticity), and are shown at 500 K potential temperature (~47–57 hPa, ~20 km). Although in this EqL band the peak in the Hunga water vapour occurred around 600 K (where the maximum anomaly reached ~3.5 ppmv, as opposed to ~1 ppmv at 500 K), results are presented at 500 K because ClO enhancements were largest there (Santee et al., 2023). Showing this surface also facilitates comparison with the stratospheric impact of the Australian New Year's (ANY) fires in late 2019/early 2020. Focusing on 2022, aerosol from the Hunga eruption began arriving in the 38°S–54°S EqL region in mid-April (Figure 5.3a), with water vapour slightly delayed, arriving in mid-June (Figure 5.3b); both then quickly and dramatically exceeded the envelope of data in all previous years. A faster aerosol sedimentation rate relative to the rate of water vapour descent in the stratospheric circulation likely explains the time difference in the onset of the enhancements (Santee et al., 2023).

Like the aerosol and water vapour, mixing ratios of the nitrogen species were fairly typical for the first few months of 2022 in this EqL range, with dinitrogen pentoxide (N_2O_5, a nighttime reservoir species for NO_x), NO_x, and HNO_3 plotted in Figures 5.3c, 5.3d, and 5.3e, respectively. However, by early June, values of N_2O_5 fell well below any previous measurements in this region by ACE-FTS. NO_x was also below average, setting new lower limits in October, November, and December. HNO_3 had a small positive anomaly in early June, with somewhat larger enhancements at higher altitudes, but the values rapidly decreased from July onward, redefining the bottom of the MLS mission envelope at some levels (Santee et al., 2023, their Figure 3). The inorganic chlorine species also showed significant perturbations due to the Hunga eruption. ClO increased rapidly beginning in early May (Figure 5.3f) at 500 K, coincident with increasing aerosol but before water vapour increased, and maintained elevated values well above the climatological range for a period of months, with peak positive anomalies in early August approaching 40 pptv. $ClONO_2$ exhibited elevated values during the intervals of ACE-FTS sampling from June to August (Figure 5.3g), coincident with the observations of enhanced ClO. Values of HCl were typical from mid-February to mid-May but dropped sharply thereafter (Figure 5.3h), falling outside the envelope of previous years for a period of months and reaching a minimum in August. N_2O did not depart from the range of previously observed variability (Figure 5.3i) but was lower than normal in the first half of the year and higher than typical in the second half. Mixing ratios of O_3 at 500 K (Figure 5.3j) were below average in 2022, similar to the behaviour in 2020 following the ANY fires, and were among the lowest values recorded by MLS in the final few months of 2022.

Based on Figure 5.3, it is clear that 2022 was an exceptional year for midlatitude stratospheric composition due to the Hunga eruption; in the 38°S–54°S EqL band, only the perturbations to chlorine species following the ANY fires in 2020 (when ClO attained peak positive anomalies of ~80 pptv) significantly separate from the climatological range prior to the eruption. Also shown in Figure 5.3 are measurements for the subsequent years 2023 and 2024. In most cases, observed compositional anomalies remain outside the background range of previous years for at least part of 2023, with 2024 values generally falling within the background envelope. The most notable exception is water vapour, which remains far higher than normal three years after the eruption.

In many cases, the peak compositional anomalies caused by the Hunga eruption occurred higher in the stratosphere and were larger in magnitude than those at 500 K (e.g., Santee et al., 2023). Figure 5.4 highlights the most significant anomalies in O_3, ClO (shown as day and night average), HCl, and HNO_3 induced by Hunga between 60°S and 60°N latitudes in 2022. To determine these values, zonal-mean, monthly average vertical profiles for each variable were calculated over 15° latitude bins using MLS data, with anomalies over the pressure range 5–60 hPa in 2022 determined relative to the previous 17 years of MLS measurements (2005–2021). Significant, widespread, and prolonged anomalies were evident in the MLS record in 2022 throughout the SH midlatitudes and tropics, and to a lesser extent, in the Northern Hemisphere (NH) tropics (Figure 5.4). Hunga had little to no significant impact on the NH midlatitudes. The dominant features in the SH are losses in O_3 and HCl, increases in ClO, and both increases and decreases in HNO_3. Focusing on the SH midlatitudes, the initial appearance of anomalies in all four species was delayed relative to that in the tropics, with the first points appearing in April or May for 30°S–45°S and July for

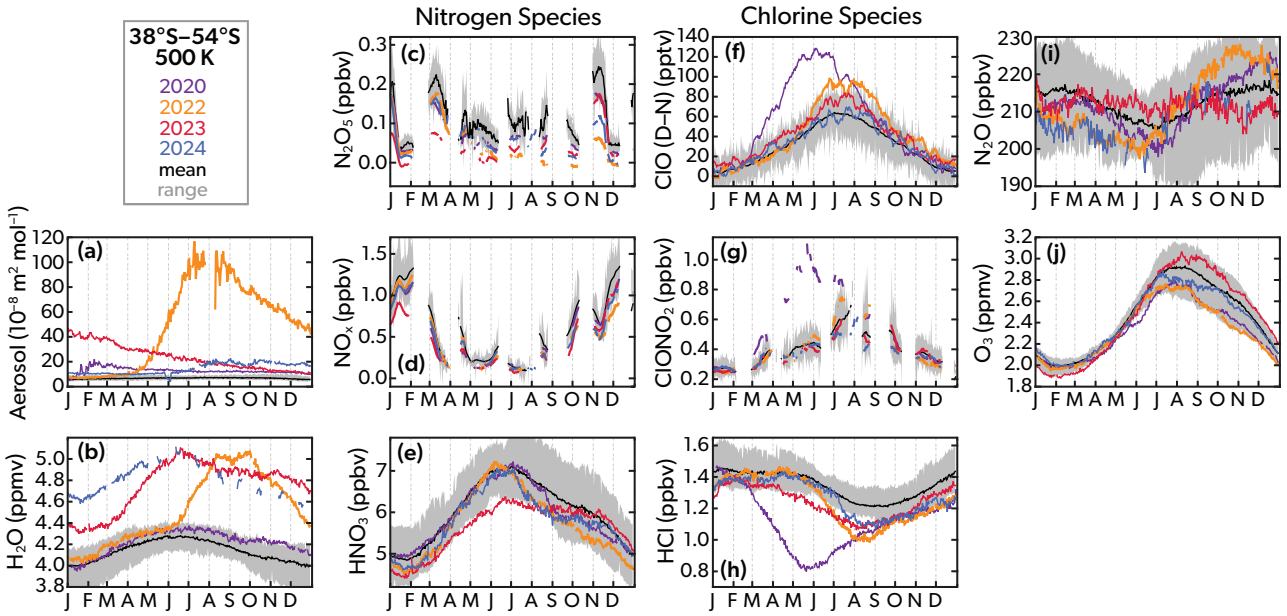

Figure 5.3: *Satellite observations averaged over 38°S–54°S EqL (SH midlatitudes) at 500 K (~47–57 hPa, ~20 km) of (a) OMPS-LP aerosol cross section at 869 nm, (b) MLS H_2O, (c) ACE-FTS N_2O_5, (d) ACE-FTS NO_x ($NO+NO_2$), (e) MLS HNO_3, (f) MLS ClO (day minus night), (g) ACE-FTS $ClONO_2$, (h) MLS HCl, (i) MLS N_2O, and (j) MLS O_3. Individual years are highlighted as indicated in the legend: 2020 in purple, 2022 in orange, 2023 in red, and 2024 in blue. Grey shading depicts the range of values observed by MLS (2005–2024), ACE-FTS (2005–2024), and OMPS-LP (2012–2024), excluding the highlighted years; black lines represent the mean of the grey-shaded data. To facilitate interpolation to isentropic surfaces, the aerosol data are converted from extinction coefficient (in units of km^{-1}) to extinction cross section per mole of air (in units of m^2 mol^{-1}), a quantity conserved under changes of atmospheric pressure in the absence of aerosol formation or loss (Santee et al., 2023). There are gaps in the 2024 MLS H_2O and N_2O data because it became necessary to duty cycle the MLS subsystem used to measure these species; thus, starting in May 2024, H_2O and N_2O measurements are available only for approximately week-long intervals in the middle of each month. ClO is shown as the day-minus-night difference to mitigate measurement bias at the lowest retrieval levels; the highlighted years and mean for ClO (but not the envelope) have been smoothed using a boxcar of width 10 days. ACE-FTS fields were also smoothed with a 10-day boxcar average. Adapted from Santee et al. (2023).*

45°S–60°S. While the largest positive anomalies in ClO and HNO_3 were observed at tropical latitudes throughout 2022, the largest negative anomalies in O_3 and HCl were observed at SH midlatitudes in the second half of the year. Peak anomalies in O_3 and HCl were −14% and −22%, respectively, relative to the previous 17-year MLS mean for the respective month and 15° latitude bin (Wilmouth et al., 2023). For HNO_3, the shift from positive to negative anomalies going from the SH tropics to the midlatitudes occurred because a higher-altitude (pressures <20 hPa) increase was replaced as the dominant feature in the vertical profile by a lower-altitude HNO_3 loss. Indeed, there was a large vertical region of HNO_3 loss, typically peaking at 31.6 hPa, from 15°S to 60°S for July to December, but it did not always satisfy the selection criteria (see the Figure 5.4 caption). Finally, considering stratospheric column ozone, record-low negative anomalies were observed at SH midlatitudes in austral spring (Wilmouth et al., 2023; Weber et al., 2024). With values calculated as monthly averages in 15° latitude bins for the 1.2–100 hPa region, the largest observed monthly anomalies in stratospheric column ozone were approximately −7% for 45°S–60°S in October and −5% for 30°S–45°S in September (Wilmouth et al., 2023).

Examination of the peak perturbations (most of which were between 20 and 40 hPa) as shown in Figure 5.4 provides a compelling picture of the substantial and persistent anomalies the Hunga eruption induced. Taken together, Figures 5.3 and 5.4 provide unmistakable evidence that changes in stratospheric composition of unprecedented magnitude and duration occurred in the SH midlatitudes following the Hunga eruption. To further elucidate the vertical structure of these changes, Figure 5.5 shows compositional anomalies in 2022 as a function of pressure for selected points in Figure 5.4. The exact MLS pressure levels of the peak perturbations in Figure 5.5 vary with latitude, month, and the species being considered, but it is ap-

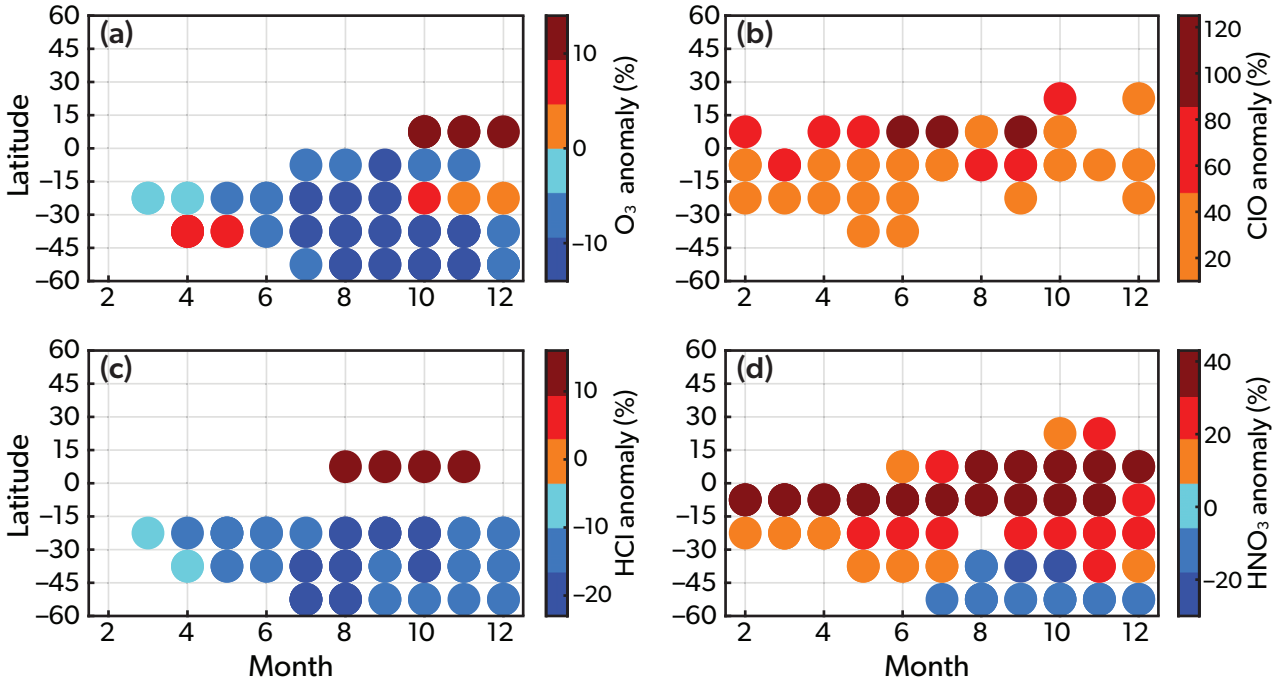

Figure 5.4: *Peak anomalies in monthly mean vertical profiles of MLS (a) O_3, (b) ClO, (c) HCl, and (d) HNO_3 for February to December 2022, labelled with the month number of the year. Note that the colour bar ranges differ for each panel, but in this figure shades of blue always indicate decreases in mixing ratio, while shades of red always indicate increases. The points are zonal-mean monthly averages over 15° latitude bins between 60°S and 60°N, with coloured circles representing the maximum outlier in mixing ratio (expressed as a percentage) over the pressure range 5–60 hPa, the region of maximum water vapour enhancement from Hunga. Only data points that satisfy the following criteria are shown: (1) mixing ratio in 2022 was greater than two standard deviations (2σ) from the 2005–2021 MLS monthly mean for the respective variable and latitude range; (2) anomaly was coincident in month, latitude bin, and pressure level with water vapour being more than 2σ above its 2005–2021 MLS mean; (3) anomaly did not already exist prior to the water vapour being elevated; and (4) anomaly persisted for more than one month. It is important to note that it is statistically possible that a few points meeting these selection criteria are not attributable to Hunga. From Wilmouth et al. (2023).*

parent that there were unprecedented enhancements in (a) ClO and (b) HNO_3 in July in the SH tropics, unprecedented reductions in (c) O_3 and (d) HCl in August at SH midlatitudes, and anomalously high (e) O_3 and (f) HCl in October in the NH tropics (Wilmouth et al., 2023). In most cases, multiple MLS pressure levels were substantially perturbed. The compositional anomalies for the months and latitudes shown in Figure 5.5 were more significant for the Hunga eruption in 2022 than for the ANY fires in 2020. The tropical anomalies are addressed further in Section 5.3.2.

The observed changes in SH midlatitude composition in the months following the eruption (as shown in Figures 5.3, 5.4, 5.5c,d) were caused by both chemistry and transport. First considering chemistry, important heterogeneous reactions in the stratosphere are summarised in Box 5.1. Reactions R5.1–R5.3 are known to be the primary cause of chlorine activation in polar winter that can lead to large Antarctic and Arctic ozone depletion, and these reactions are enhanced in the presence of elevated volcanic sulfate aerosol and water vapour. However, CCM simulations with SOCOL-AERv2-Volc (SOCOL = modeling tools for studies of SOlar Climate Ozone Links, AER = 2-D aerosol model, Volc = heat flux, mixed-layer ocean, and SSP implementation; Wilmouth et al., 2023) and rate constant analyses (Santee et al., 2023) show that even though these reactions are faster following the Hunga eruption, all three are too slow at temperatures in the middle stratosphere to have played any significant role in driving the observed compositional changes in 2022.

Reactions R5.4 and R5.5 are enhanced following the Hunga eruption and, unlike R5.1–R5.3, they are relatively insensitive to temperature. Indeed, the N_2O_5 hydrolysis reaction (R5.4) on elevated sulfate aerosol was the dominant heterogeneous reaction driving chemical changes following the Hunga eruption (Santee et al., 2023; Wilmouth et al., 2023; Zhang et al., 2024a; Bednarz et al., 2025), as it was following

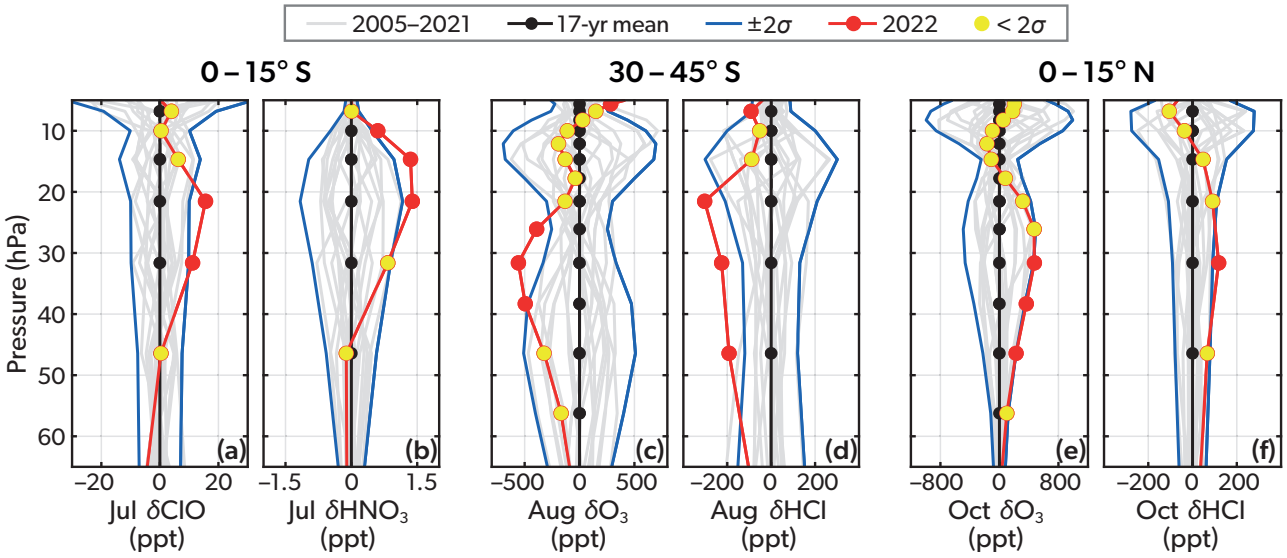

Figure 5.5: *Anomalies in the monthly mean vertical profiles of selected MLS measurements for each year from 2005 to 2022 relative to the 2005–2021 mean value. Mixing ratio anomalies are shown for (a) ClO and (b) HNO_3 for July at 0°–15°S, (c) O_3 and (d) HCl for August at 30°S–45°S, and (e) O_3 and (f) HCl for October at 0°–15°N. All longitudes are included in the averages. Data for each of the 17 years from 2005–2021 are shown in grey, the 17-year mean is shown in black, lines representing ±2σ from the 17-year mean are shown in blue, data points from 2022 that fall inside the 2σ lines are plotted in yellow, and data from 2022 outside the 2σ lines are shown in red. Adapted from Wilmouth et al. (2023).*

the Mount Pinatubo eruption (e.g., Fahey et al., 1993; Kinnison et al., 1994). It is noteworthy that the chemical changes induced by the N_2O_5 hydrolysis reaction would have been even more substantial had this reaction not reached saturation (Santee et al., 2023). Saturation occurs because N_2O_5 formation (mainly from NO_2+NO_3 at night) is slower than Reaction R5.4 when stratospheric aerosol loading is sufficiently elevated, i.e., N_2O_5 is hydrolysed as fast as it can be formed. The bromine nitrate ($BrONO_2$) hydrolysis reaction (R5.5), when coupled with a subsequent heterogeneous reaction of hypobromous acid (HOBr) with HCl (R5.6), has also been suggested to play a significant role in the chemical loss of HCl following the Hunga eruption (Zhang et al., 2024b; Bednarz et al., 2025).

In addition to heterogeneous reactions, gas-phase reactions were significantly impacted (e.g., Santee et al., 2023; Wilmouth et al., 2023; Zhang et al., 2024b). Because the chemical cycles controlling stratospheric composition are highly interconnected, perturbations in even just one or two reactions can have far-reaching impacts. The manner in which enhanced HNO_3, decreased NO_x, and elevated OH impact other chemical cycles has been discussed in detail (Santee et al., 2023; Wilmouth et al., 2023). Here, it is sufficient to summarise that ozone-loss cycles involving HO_x and ClO_x are enhanced, while NO_x-driven ozone loss slows (e.g., Zhang et al., 2024a, their Figure 3c; Fleming et al., 2024, their Figure 9b; Bednarz et al., 2025). For some of the measurements shown in Figures 5.3–5.5, the impact of altered chemistry following Hunga is clear, particularly in the record-low N_2O_5 and NO_x and record-high ClO. In other cases, such as HNO_3, HCl, and O_3, chemistry is only part of the story, and transport must be considered.

The cooling effect of the greatly elevated stratospheric water vapour following the Hunga eruption caused changes in stratospheric circulation (see Chapter 4) that led to some of the observed changes in composition. The importance of altered transport for trace-gas distributions has been demonstrated with both tracer–tracer correlations (Santee et al., 2023; Wilmouth et al., 2023) and atmospheric modelling (Wang et al., 2023; Zhang et al., 2024a; Bednarz et al., 2025). The method used in independent tracer analyses was to evaluate correlations in the anomalies of HNO_3, HCl, and O_3 with anomalies in nitrous oxide (N_2O), as N_2O represents a long-lived tracer for large-scale transport in the atmosphere. These tracer–tracer analyses (Santee et al., 2023; Wilmouth et al., 2023) showed that changes in transport were the primary factor in causing the observed anomalies in HNO_3, HCl, and O_3 mixing ratios, particularly at SH midlatitudes in the second half of 2022. For example, the dominant role of transport explains why HNO_3 decreases in the second half of 2022 in Figure 5.3e des-

pite Reaction R5.4, while the importance of chemistry is revealed by a plot of HNO_3/NO_y (odd nitrogen, $NO_y \approx 2\times N_2O_5 + NO_x + HNO_3 + ClONO_2$) showing record-high values over that same time period (Santee et al., 2023, their Figure 2), suggesting heterogeneous HNO_3 production. Similarly, the strong SH midlatitude reductions in O_3 and HCl shown in Figures 5.3j and 5.3h (seen also in Figures 5.5c,d) correlate with high values of N_2O (Figure 5.3i). In short, several analyses (Santee et al., 2023; Wilmouth et al., 2023; Zhang et al., 2024b) indicated that changes in transport played the more important role in perturbing HCl, HNO_3, and O_3 mixing ratios in the SH midlatitudes, but chemical perturbations were also significant, especially for HCl. Of these three, anomalies in ozone showed the smallest chemical signature (Santee et al., 2023; Wilmouth et al., 2023). A WACCM6 modelling study quantified the ozone loss due to chemistry to be ~4% at SH midlatitudes near ~70 hPa in August 2022, compared to a maximum modelled ozone loss of ~15% at 30–50 hPa due to combined dynamical and chemical influences. The chemical loss may be underestimated, as the simulations did not include the dynamical feedback on chemistry (Zhang et al., 2024a). On the other hand, a recent analysis of ensembles of multi-model CCM simulations performed as part of HTHH-MOC found that the chemical perturbations induced by Hunga were comparable in importance to the changes in transport in determining the overall ozone response to the eruption in the SH extratropics (Bednarz et al., 2025).

The observed anomalies in stratospheric composition following the Hunga eruption in 2022 were of distinctly different origin than the anomalies in 2020 (Santee et al., 2022; Strahan et al., 2022), when the high solubility of HCl in aged stratospheric smoke particles from the ANY fires apparently prompted heterogeneous chlorine activation via Reaction R5.2, leading to larger perturbations in chlorine partitioning (Solomon et al., 2023). While the details of the Mount Pinatubo (e.g., Kinnison et al., 1994; Aquila et al., 2013) and Hunga eruptions differ substantially, they were similar in that the significant and prolonged changes in stratospheric composition that followed were caused by a combination of altered chemistry and transport.

5.3.2 Tropics

Evidence from satellite observations reveals substantial impacts of the Hunga eruption on chlorine and nitrogen chemistry in the tropical stratosphere (Santee et al., 2023; Wilmouth et al., 2023). While perturbations in the abundances of those species were remarkable for the tropics, they were too small to affect ozone in the lower stratosphere to a significant degree. Evolution of ozone in that layer was instead dominated by transport. However, in the second half of 2022, anomalous nitrogen partitioning triggered by the eruption suppressed the NO_x catalytic loss cycle, resulting in a notable increase in middle-stratospheric ozone.

The impacts on composition were seen in the tropics several months before they were evident at midlatitudes (Figure 5.4), consistent with the evolution of the water vapour and aerosol (see Chapter 3). Similar to the situation in the SH midlatitudes, the perturbations of the ClO_x, NO_x, and HO_x species were significant (Santee et al., 2023; Wang et al., 2023; Fleming et al., 2024). Peak ClO anomalies (Figure 5.4b) were positive in the tropics throughout the year, with ClO abundances reaching up to twice their climatological values in June, July, and September 2022. There is a consistent pattern of high maximum HNO_3 abundances throughout 2022 (Figure 5.4d), as well as more moderate peak HCl values north of the equator and negative values between 15°S and 30°S (Figure 5.4c). Peak O_3 anomalies in the tropics in 2022 were mostly negative, except in the latter part of the year starting in October (Figure 5.4a).

The vertical structure of some of these anomalies is shown in Figure 5.5. The maximum ClO enhancements of over two standard deviations (2σ) from the climatological mean in the latitude band 0°–15°S in July occurred near 20 hPa (~26.5 km; Figure 5.5a). When adjusted for trends and dynamical variability, large increases in ClO due to chemistry were also observed in the upper stratosphere up to about 36.5 km (4.6 hPa) in 2023 (Nedoluha et al., 2025, not shown here). The ClO enhancements in the upper stratosphere were attributed to increased OH from the additional water vapour. HNO_3 mixing ratios exceeded the 2σ threshold in a broad layer between 30 hPa and 10 hPa (~24–31 km; Figure 5.5b). In October, positive maximum ozone and HCl anomalies immediately north of the equator occurred at altitudes below (i.e., pressures greater than) 30 hPa (~24 km; Figures 5.5e,f). The presence of strongly negative N_2O anomalies at the same time and altitudes (Wilmouth et al., 2023, their Figure S14) suggests that transport was the direct driver of the high HCl and ozone in that latitude band. It is not known whether radiative effects of the Hunga eruption were responsible for

this circulation anomaly in the tropics (see Chapter 4).

Chlorine and nitrogen chemistry in 2022 was dominated by the hydrolysis of N_2O_5 (Reaction R5.4) on volcanic sulfate aerosol and subsequent gas-phase reactions (Santee et al., 2023). This is different from the typical pathway of heterogeneous chlorine activation in the winter polar lower stratosphere, which involves reactions between chlorine reservoir species (R5.1–R5.3). At 620 K (~26 hPa, ~25 km), the level where the initial enhancements in water vapour from the eruption were maximum in the tropics, there was a rapid initial increase in HNO_3 and ClO, concomitant with a drop in N_2O_5 and NO_x (Figures 5.6c–f). The 2022 values redefine the envelopes of previously observed abundances for these four species based on data collected between 2005 and 2021. The timing of those initial changes closely followed the increases in water vapour and aerosols in the tropics in late January 2022 (Figures 5.6a,b). A more moderate increase in $ClONO_2$ and a decrease in HCl (Figures 5.6g,h) are also seen. Evidence for N_2O_5 hydrolysis being the primary mechanism of this repartitioning of chlorine and nitrogen species is provided by the subsequent evolution of HNO_3 and ClO. Specifically, after the rapid initial increase, HNO_3 mixing ratios reached a plateau between March and May 2022 and then followed their typical seasonal trajectory while remaining about 10% above the mean. This March–May plateau is also seen in HNO_3 anomalies at other altitudes (Santee et al., 2023, their Figure 8). After reaching its maximum anomaly in mid-March, ClO was also roughly constant through May, after which values declined slowly while remaining significantly higher than average throughout most of 2022. The fact that the rise in the abundances of these gases stalled in late February or March despite the continuing increases in aerosol and water vapour loading, combined with an increase in $ClONO_2$ (rather than a decrease, as would be expected if direct heterogeneous chlorine activation Reactions R5.2 or R5.3 were at work), suggests that it was N_2O_5 hydrolysis, which is subject to saturation, that dominated their production.

The evolution of ozone in the tropical lower stratosphere in 2022 was mainly driven by transport. Ozone mixing ratios were mostly above average at 620 K (~26 hPa, ~25 km), with significant up- and downswings throughout the year (Figure 5.6j), suggesting that the chlorine activation had only a limited impact on ozone at that level, and any chemical loss that might have occurred was masked by much stronger dynamical variability. This assertion is strengthened by a quantitative analysis of the perturbations in chlorine chemistry. As exceptional as they were, the ClO enhancements in the tropics in 2022 were still more than an order of magnitude weaker than those during a typical polar winter. For example, the maximum ClO enhancements observed between 22°S and 6°S EqL following the Hunga eruption were about 0.04 ppbv (Figure 5.6f), compared to at least 1 ppbv observed in the lower stratosphere over the Antarctic in September (World Meteorological Organization (WMO) (2022); see also Section 5.3.3).

Mixing ratios of the transport tracer, N_2O, were low between February and June 2022 (Figure 5.6i), suggesting anomalously slow tropical upwelling consistent with the observed circulation anomalies in 2022. However, it is difficult to determine how much of this transport anomaly resulted from the eruption, given strong interannual and quasi-biennial oscillation (QBO) variability in tropical upwelling (see Chapter 4). Examination of joint distributions of chemically active gases and N_2O provides further insights into the relative importance of chemistry and transport for the observed composition anomalies in 2022 (Figure 5.7). Based on MLS data between 2005 and 2021, both the N_2O/HNO_3 and N_2O/HCl anomaly distributions exhibit compact relationships (Figures 5.7a–c and 5.7d–f, respectively). This reflects the relatively long chemical lifetimes of these species in the lower stratosphere. Consequently, deviations from the climatological distributions indicate anomalous chemical production or loss. The HNO_3 values in the broad layer between 580 K and 660 K are slightly outside of the 2005–2021 envelope between February and July 2022, consistent with chemical processing, as discussed above. HCl mixing ratios at and above 620 K between July and October 2022 are lower than can be explained by transport, providing further evidence for heterogeneous chemical processing, consistent with highly elevated HNO_3 and ClO. Correlations between N_2O and ozone (Figures 5.7g–i) are weaker than those for HNO_3 and HCl, but the joint distributions of these gases still provide insights into mechanisms responsible for tropical ozone anomalies in 2022. At 620 K and 580 K (~32 hPa, ~24 km; Figures 5.7h,i), ozone anomalies are within previously observed ranges. The lack of significant departure from the climatological N_2O/O_3 relationship supports the conclusion stated earlier that no substantial chemical ozone loss occurred at that level. A clearer chemical signal is present at 660 K (~22 hPa, ~26 km; Figure 5.7g) and above (not shown), where ozone anomalies reached

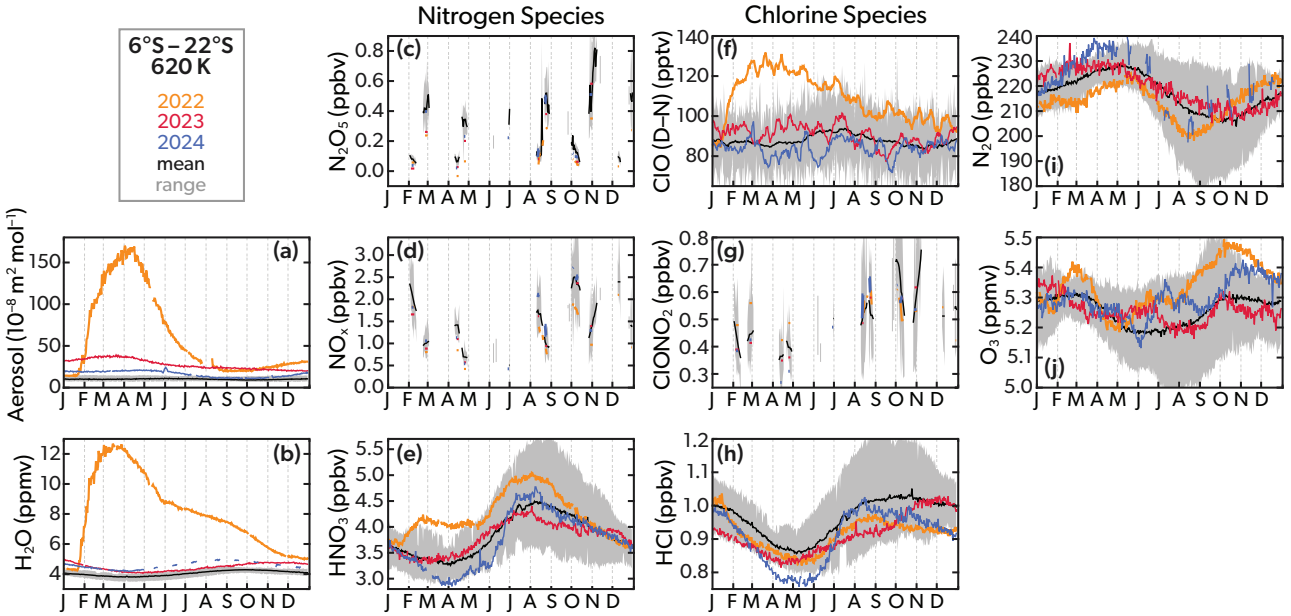

Figure 5.6: *Satellite observations averaged over 6°S–22°S EqL (SH tropics) at 620 K (~26 hPa, ~25 km) of (a) OMPS-LP aerosol cross sections at 869 nm, (b) MLS H_2O, (c) ACE-FTS N_2O_5, (d) ACE-FTS NO_x, (e) MLS HNO_3, (f) MLS ClO (day minus night), (g) ACE-FTS $ClONO_2$, (h) MLS HCl, (i) MLS N_2O, and (j) MLS O_3. Individual years are highlighted as indicated in the legend: 2022 in orange, 2023 in red, and 2024 in blue. Grey shading depicts the range of values observed by MLS (2005–2024), ACE-FTS (2005–2024), and OMPS-LP (2012–2024), excluding the highlighted years; black lines represent the mean of the grey-shaded data. To facilitate interpolation to isentropic surfaces, the aerosol data are converted from extinction coefficient (in units of km^{-1}) to extinction cross section per mole of air (in units of m^2 mol^{-1}), a quantity conserved under changes of atmospheric pressure in the absence of aerosol formation or loss (Santee et al., 2023). There are gaps in the 2024 MLS H_2O and N_2O data because it became necessary to duty cycle the MLS subsystem used to measure these species; thus, starting in May 2024, H_2O and N_2O measurements are available only for approximately week-long intervals in the middle of each month. ClO is shown as the day-minus-night difference to mitigate measurement bias at the lowest retrieval levels; the highlighted years and mean for ClO (but not the envelope) have been smoothed using a boxcar of width 10 days. ACE-FTS fields were also smoothed with a 10-day boxcar average. Adapted from Santee et al. (2023).*

record-high values in the second half of the year (see also Figure 5.6j). The absence of corresponding large anomalies in N_2O suggests that this ozone enhancement is not readily explained by transport. Rather, the elevated ozone abundances are consistent with anomalously low NO_x abundances (Figure 5.6d) and the resulting suppressed chemical loss from the catalytic NO_x cycle.

Ensemble simulations using the 3-D global CCM SOCOL-AERv2-Volc with injected water vapour and SO_2 leading to water vapour and sulfate aerosol enhancements reflecting those from the eruption produce responses in stratospheric composition in the tropics (0°–30°S) that are in qualitative agreement with observations in April 2022 (Wilmouth et al., 2023). The model simulation finds enhanced HO_x, HOCl, HNO_3, and ClO and reduced HCl, NO_x, and N_2O_5 compared to a control experiment. Modelled O_3 and ClO closely agree with MLS observations. Qualitative agreement between modelled and measured HCl and HNO_3 is also seen, although the model overestimates the observed HNO_3 enhancement and the reduction in HCl (Wilmouth et al., 2023). In addition, these simulations show significant changes in chemically active compounds unobserved from space; in particular, they produce peak increases of 50% for HO_x and 100% for HOCl.

Finally, we briefly discuss the composition of the tropical stratosphere in the years following 2022. While water vapour and aerosols remained elevated throughout 2023 and 2024, HNO_3, ClO, HCl, and ozone largely returned to their climatological abundances in 2023 (Figures 5.6e,f,h,j). N_2O_5 remained low through April 2023 but was well within its climatological envelope in the latter part of the year (Figures 5.6c,d). Between March and July 2024, HCl, $ClONO_2$, and HNO_3 reached record or near-record low values. The origin of these anomalies is not known, but a corresponding strong positive anomaly in N_2O (Figure 5.6i) suggests that they may have

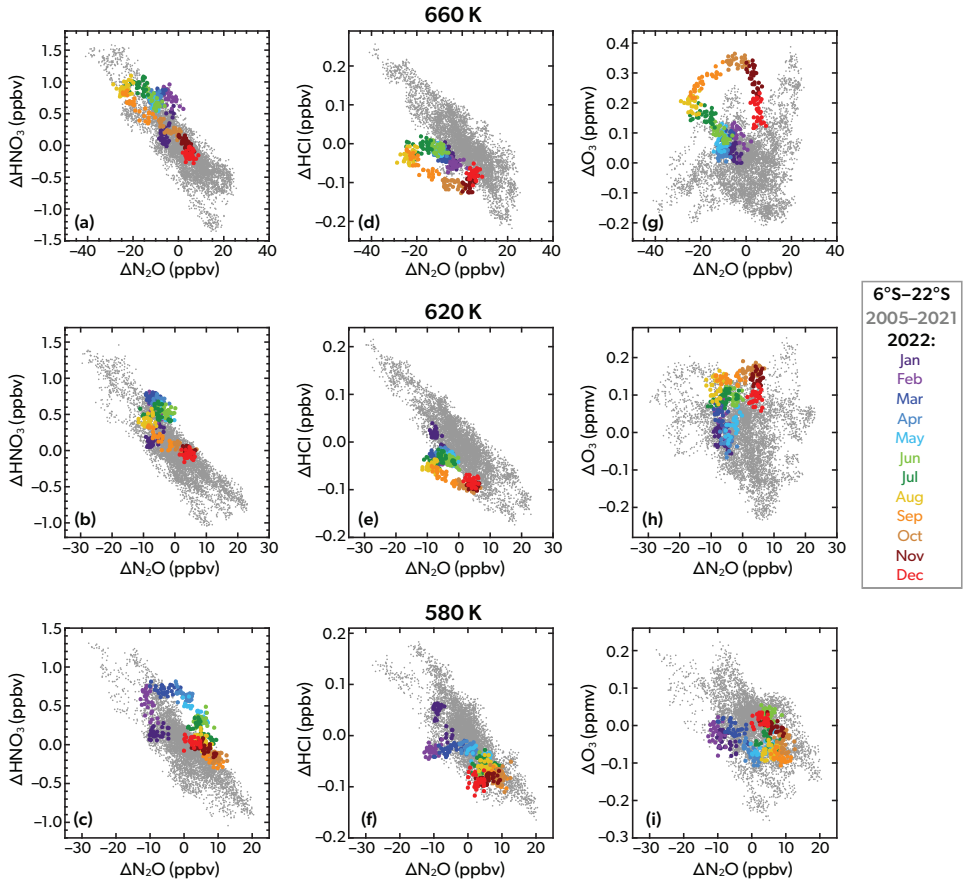

Figure 5.7: *Scatter plots of daily N_2O anomalies versus anomalies of HNO_3 (a–c), HCl (d–f), and O_3 (g–i) from MLS observations averaged between 6°S and 22°S EqL at selected potential temperature levels: 660 K (~22 hPa, ~26 km; a, d, g), 620 K (~26 hPa, ~25 km; b, e, h), and 580 K (~32 hPa, ~24 km; c, f, i). Data from 2005–2021 are shown in grey; 2022 data are coloured by month as indicated by the legend. Adapted from Santee et al. (2023).*

been transport related. Ozone, on the other hand, is generally only weakly correlated with N_2O at the altitude considered here (Figure 5.7h). It was close to its long-term average during the first half of 2024 and above average for the rest of the year, with the exception of September (Figure 5.6j).

5.3.3 Antarctic winters/springs of 2022, 2023, and 2024

Antarctic winter/spring of 2022 The Hunga eruption had minimal impact on Antarctic stratospheric polar chemistry in 2022. The 2022 austral winter polar vortex was large, cold, and stable, and its dynamical characteristics were well within the range of pre-Hunga values (Figure 5.8; Manney et al., 2023; Wargan et al., 2025). A small increase in aerosol loading was observed at high southern latitudes in the lowermost stratosphere (430 K and below) before the vortex had fully formed at those levels (Khaykin et al., 2022; Taha et al., 2022; Manney et al., 2023). In contrast, the Hunga water vapour was effectively excluded from the 2022 Antarctic vortex by the strong transport barrier at the vortex edge (Schoeberl et al., 2022; Manney et al., 2023), and water vapour was not fully entrained into the deep branch of the Brewer–Dobson circulation (BDC) until 2023 (Zhou et al., 2024); see Chapter 3. While some observational studies showed evidence that the heterogeneous chemical processing (chlorine activation, denitrification, dehydration) and ozone loss that took place within the vortex were near average (Figure 5.8; Manney et al., 2023), others reported Antarctic polar-cap-averaged observed (and simulated) ozone abundances with values in October that were ~30% less than typical, though still within the climatological range (Wang et al., 2023; Fleming et al., 2024; Zhang et al., 2024a; Zhou et al., 2024). This apparent inconsistency may be explained by the studies' examination of averages calculated over different regions of interest—geographic latitude bands vs. the vortex. The dynamical characteristics (e.g., size, shape, and position) of the Antarctic vortex are highly variable; since polar-cap (i.e., 60°S–90°S)

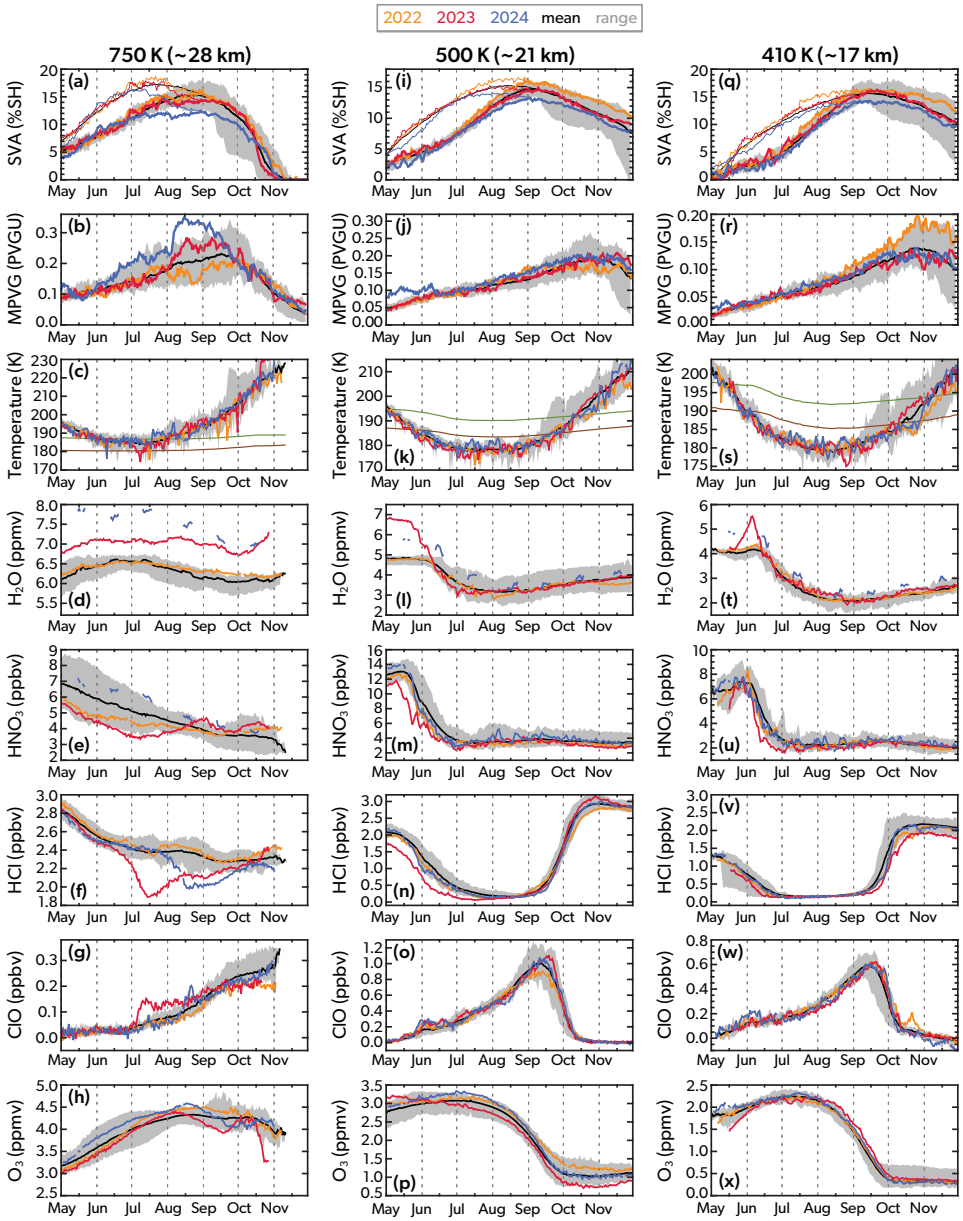

Figure 5.8: *Time series from May through November of daily quantities in the SH polar region on three selected isentropic surfaces: 750 K (left), 500 K (middle), and 410 K (right). For all panels, grey shading depicts the range of observed values and black lines the mean over 2005–2021. The coloured lines represent different years as indicated in the legend: 2022 (orange), 2023 (red), and 2024 (blue). (a, i, q) MERRA-2 Antarctic total vortex area (thinner lines) and sunlit vortex area (SVA, thicker lines), both expressed as a percentage of the hemisphere (%SH). SVA is smaller than the total vortex area for the first few months, as a portion of the vortex remains in darkness, but later in the season the two curves converge. Vortex area calculations require definition of the approximate "edge" of the polar vortex, identified here using specified contours of scaled potential vorticity (PV) that vary with altitude, as described by Lawrence et al. (2018). The total vortex area envelope is omitted for clarity. (b, j, r) MERRA-2 maximum scaled-PV gradient (MPVG, a measure of vortex strength), in units of 10^{-4} s^{-1} deg^{-1} (PVGU). (c, k, s) MLS minimum temperatures inside the vortex. Thinner lines mark the formation thresholds for HNO_3-containing (green) and water-ice (brown) PSCs, respectively. (d, l, t) Vortex averages of MLS H_2O. There are gaps in the 2024 data because it became necessary to duty cycle the MLS subsystem used to measure H_2O; thus, starting in May 2024, H_2O measurements are available only for approximately week-long intervals in the middle of each month. Vortex averages of (e, m, u) HNO_3, (f, n, v) HCl, (g, o, w) daytime-only ClO, and (h, p, x) O_3. Adapted from Santee et al. (2024).*

averages do not account for undulations of the vortex edge, they inevitably mix inside- and outside-vortex air, especially after September, when stronger dynamical variability in austral spring increasingly confounds signatures of chemical ozone loss. Modelled chemical impact on Antarctic ozone from the excess Hunga water vapour was found to be negligible using the TOMCAT CTM (Zhou et al., 2024), and the low polar-cap-averaged ozone was largely attributed to internal variability in the climate system and dynamical changes that may have been forced by the eruption based on WACCM6 results (Wang et al., 2023; Zhang et al., 2024a). After the vortex broke down in November–December 2022, enhanced stratospheric water vapour and aerosols pervaded the southern middle and high latitudes (Manney et al., 2023) and persisted into 2023. Thus it was extraordinarily humid over the Antarctic when the 2023 vortex formed, and concentrations of large aerosol particles (with diameters greater than 0.5 μm) were also greatly increased (by as much as an order of magnitude; Deshler et al., 2024).

Antarctic winter/spring of 2023 As in 2022, the 2023 Antarctic polar vortex was large, stable, and cold. Dynamical characteristics (such as the maximum gradient in scaled potential vorticity, a measure of vortex strength) were generally unremarkable and, along with vortex temperature, within climatological norms (Figure 5.8; Santee et al., 2024; Zhou et al., 2024; Wargan et al., 2025). However, relatively weak planetary-scale wave activity from mid-October onwards slowed the seasonal transition to summer, with the breakdown of the vortex delayed until mid-December, nearly two weeks later than usual (Kramarova et al., 2024). The prolonged duration of the 2023 Antarctic lower stratospheric vortex was similar to that of the prior three years (2020–2022), which also saw weaker-than-average wave activity in late austral spring (Kramarova et al., 2024).

Water vapour was exceptionally high at the start of austral winter in May, 10–40% higher than normal over much of the stratosphere (Figures 5.8d,l,t; Santee et al., 2024; Wohltmann et al., 2024), and the vortex remained unusually moist throughout 2023 at altitudes at and above 600 K (e.g., Figure 5.8d). Enhanced water vapour abundances both reduced vortex minimum temperatures by ~1–2 K (within the climatological range) in early winter (June; Fleming et al., 2024) and raised the threshold temperatures for the formation of water ice and HNO_3-containing polar stratospheric clouds (PSCs) by ~1–2 K above typical values (Santee et al., 2024; Wohltmann et al., 2024). The cold, humid conditions caused earlier (May) and more extensive PSC formation than usual. Ice PSC volume in late June was the largest ever observed by CALIOP, estimated at ~55 million km^3 (compared to the mission average of ~20 million km^3; Figure 5.9a). Such an increase in ice PSC abundance was predicted in model simulations considering the Hunga hydration (Fleming et al., 2024; Zhou et al., 2024). HNO_3-containing PSC volume in late June was also elevated but within climatological variability (Figure 5.9b). Consistent with these results, the season-integrated volume of PSC occurrence inferred from (daytime-only) OMPS-LP aerosol measurements was the largest in the 13-year OMPS-LP record (DeLand and Schoeberl, 2025).

The availability of excess water vapour above the saturation limit might be expected to produce larger particles with correspondingly greater sedimentation velocity (Wohltmann et al., 2024). ACE-FTS aerosol observations in September and October 2023 support this hypothesis, as inferred aerosol sulfate radius was the largest ever reported (Lecours et al., 2024). Extensive PSC sedimentation caused early-season (May–June) large-scale dehydration and denitrification of the lower stratospheric vortex. It was estimated that ice PSC sedimentation removed ~35 Tg of water vapour from the stratosphere in 2023, compared to ~23 Tg in a typical Antarctic winter (Millán et al., 2024). By mid-July, water vapour in the lower stratosphere was "reset" back to the typical range (3–4 ppmv) observed in earlier years and essentially followed the climatological mean thereafter (Figures 5.8l,t). In other words, the dehydration process had run to completion by mid-winter (July–August). Substantial hydration (of ~1 ppmv) from evaporation of ice particles falling from above also occurred over 380–460 K (~102–46 hPa, ~15–19 km) in the lower stratosphere in late May/early June (e.g., Figure 5.8t); such PSC-related hydration had not been previously reported as early in the season or at as high altitudes as observed in 2023 (Santee et al., 2024). Rapid denitrification of the vortex occurred in May and June 2023 (see the sharp declines in HNO_3 in Figures 5.8e,m,u). However, as with water vapour, HNO_3 evolution mostly followed the climatological mean after mid-July, indicating that the denitrification process had run its course. Ground-based remote-sensing measurements of HNO_3, NO, and NO_2 made at Arrival Heights, Antarctica, confirm that Hunga did not cause excess denitrification during the 2023 season

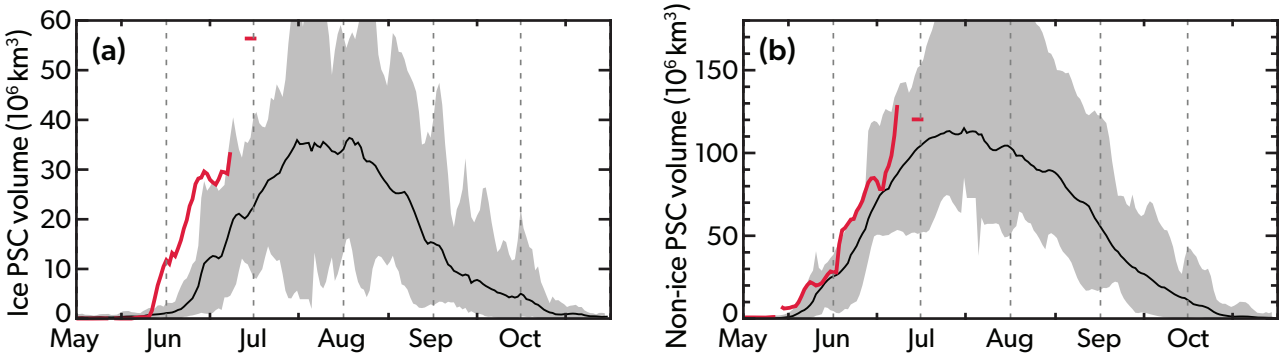

Figure 5.9: *Daily values of Antarctic (a) ice and (b) HNO_3-containing (liquid and solid, labelled as "non-ice") PSC spatial volumes, calculated by integrating PSC areal coverage values over the altitude range 12–30 km, derived from the CALIOP cloud mask product. These time series terminate at the end of October, as PSC activity typically ceases by that time. Grey shading depicts the range of values from the climatology of PSC volume, and black lines show the mean over 2006–2022 (excluding 2023, shown in red). Regular daily CALIOP measurements ceased in late June 2023; therefore, PSCs were observed directly only during the early part of the 2023 Antarctic winter. Adapted from Santee et al. (2024).*

(Smale et al., 2025).

Unprecedented early-winter chlorine activation was seen at higher altitudes of 600–800 K (~18–8 hPa, ~25–30 km), where record-low HCl (Figure 5.8f) and an associated increase in ClO (Figure 5.8g) were observed in June–August 2023. Early and moderately strong chlorine activation was observed in the layer around 500 K as well (Figures 5.8n,o). Such anomalous chlorine activation in early winter is a consequence of increased PSC surface area, lower temperatures, and enhanced water vapour causing a faster rate of Reaction R5.2 (Fleming et al., 2024). However, by the end of July, HCl and ClO mixing ratios throughout the lower stratosphere were within their usual ranges. Thus, while chlorine activation was observed earlier in the winter than usual, HCl depletion and ClO enhancement eventually plateaued due to saturation of heterogeneous chemical processing (irrespective of elevated water vapour and PSC abundances) within the vortex core. Consistent with lingering below-average temperatures (Figures 5.8k,s), chlorine deactivation was slightly delayed throughout the lower stratosphere, with enhanced ClO persisting longer than usual into mid-September and then dropping to near-average values from October onwards (Figures 5.8o,w). Chlorine species measured at the Arrival Heights ground station also indicate persistent chlorine activation in September 2023 (Smale et al., 2025).

Although the early-winter chlorine activation at 600–800 K temporarily redefined the envelope of behaviour, the ClO enhancement in that layer was still nearly an order of magnitude smaller than that seen in the sunlit vortex later in the season at lower altitudes (~500 K) and thus was too weak to induce substantial ozone depletion. The August–September decrease in ozone at 750 K was tentatively ascribed to destruction induced by solar energetic particles, rather than chemical processing on PSCs, while the sharp decline in late October was attributed primarily to descent of ozone-poor air from higher potential temperatures (Figure 5.8h; Santee et al., 2024). At 500 K, the persistence of very high ClO abundances (and thus strong chemical loss) likely brought about the low ozone mixing ratios at the end of the winter at that level (Figure 5.8p; Santee et al., 2024). At 410 K, ozone remained at or above the climatological mean through most of the season (Figure 5.8x).

Chemical ozone destruction is quantified in several ways. One approach is "MLS-Match," whereby trajectory calculations are used to identify air parcels sampled multiple times by MLS to account for transport effects. The MLS-Match analysis in a study by Santee et al. (2024) covered the period from 1 May through 15 October, chosen to encompass the bulk of the chemical ozone destruction while excluding the much greater dynamical variability at the end of the season; similar results were obtained employing the MLS-Match method over 1 June–30 September by Wargan et al. (2025). At the upper levels (600–800 K), the MLS-Match–derived cumulative amount of ozone destroyed over the course of the winter (~1 ppmv or less) was only slightly above average and well within the typical range (Figure 5.10a; Santee et al., 2024). At 410–550 K (~74–24 hPa, ~17–23 km) in the lower stratosphere, cumulative chemical ozone losses were relatively large (~2.3–3.6 ppmv, depending on level) but not unprecedented (Figure 5.10a). Integrating the MLS-Match height-resolved cumu-

lative chemical ozone changes over the vertical domain from 375 to 900 K yielded an estimate of vortex-averaged stratospheric partial column ozone loss for 2023 that was ~2 DU less than the 2005–2022 MLS mission mean estimated partial column loss, well within the observed year-to-year variability (Santee et al., 2024). In another study, subtracting from the MLS ozone values a modelled passive ozone tracer initialised on 1 June using the ATLAS CTM yielded somewhat smaller estimates of observed vortex-averaged ozone loss on 1 October of ~1.5–2.6 ppmv in the lower stratosphere (Wohltmann et al., 2024). The modelled vortex-averaged stratospheric partial column (133.4–23.7 hPa) ozone loss, calculated by subtracting from modelled ozone fields the modelled passive ozone tracer, underestimated the MLS-derived loss by about 30% (Figure 5.10b). While ATLAS ozone abundances in the lower stratosphere were significantly higher than those observed by MLS in 2023 (Wohltmann et al., 2024, their Figure 2), better agreement between ATLAS and MLS ozone is seen in other Antarctic winters. A possible explanation for the larger model/measurement discrepancy in 2023 is that water vapour is not assimilated in the ECMWF ERA5 reanalysis used to drive the model. Since post-eruption ERA5 water vapour abundances deviated substantially from observed values, the representation of vertical transport in the vortex in ERA5 (and thus the modelled passive ozone tracer) may be unrealistic in 2023.

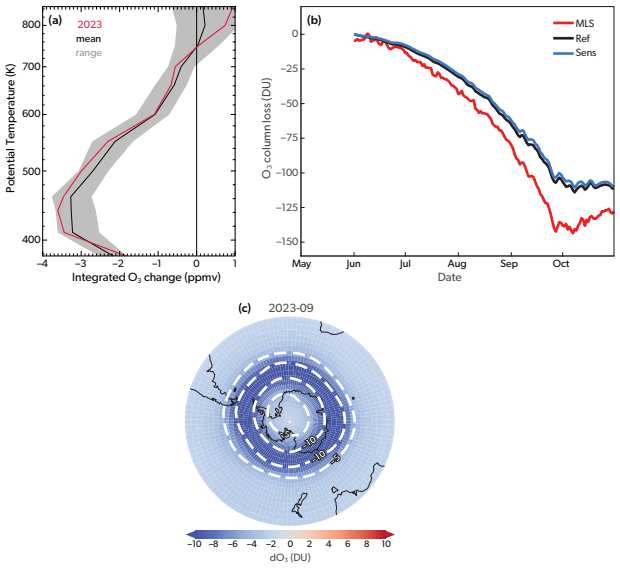

Figure 5.10: *(a) Vertical profiles of vortex-averaged chemical ozone change from the MLS-Match analysis integrated over the Antarctic winter from 1 May to 15 October. Grey shading depicts the range of values and the black line the climatological mean over 2005–2022; the red line denotes 2023 values. Adapted from Santee et al. (2024). (b) Temporal evolution of vortex-averaged chemical loss of ozone for the partial column from 133.4–23.7 hPa (~360–550 K, ~13–23 km) in 2023. Chemical ozone loss was determined by subtracting a passive ozone tracer initialised on 1 June from modelled and measured ozone values. The black line shows modelled results from the reference run ("Ref") initialised with MLS measurements from 2023, while the blue line shows modelled results from a sensitivity run ("Sens") initialised with MLS water vapour data from 2022 (i.e., without the effect of Hunga on water vapour), utilising the 3-D CTM ATLAS. The difference between the Ref and Sens runs quantifies the ozone loss attributable to the Hunga-induced increase in water vapour. The red line quantifies the observed chemical ozone loss through subtraction of the passive ozone tracer from the ozone values observed by MLS in 2023 and shows that the CTM (ATLAS) consistently underestimates ozone loss compared to MLS. Adapted from Wohltmann et al. (2024). (c) Modelled monthly mean difference in column ozone between a control simulation and one including the Hunga hydration for September 2023 using the 3-D CTM TOMCAT. White dashed lines mark the −5 and −10 DU contours. Adapted from Zhou et al. (2024).*

Modelling studies have generally found weak impacts from the Hunga hydration on the 2023 Antarctic ozone hole. The chemical ozone loss attributable to the eruption was quantified by comparing simulations with and without the Hunga water vapour perturbation. Subtracting a passive ozone tracer from simulated ozone fields from the ATLAS CTM, the direct effect of the excess water vapour on modelled vortex-averaged stratospheric partial column ozone loss was found to be less than 4 DU, compared to ~145 DU of loss in the vortex-averaged stratospheric partial column estimated from MLS measurements (Figure 5.10b; Wohltmann et al., 2024). TOMCAT simulations indicated Hunga-induced column ozone loss of ~10 DU (~4% of the background) over June–September 2023, with most of the additional loss occurring in the collar region along the vortex edge (Figure 5.10c; Zhou et al., 2024; Smale et al., 2025), where chlorine is typically not fully activated. Projections by the NASA GSFC2D model indicated that Hunga exacerbated polar-cap-average column ozone loss in 2023 by 13–23 DU, depending on the planetary wave driving scenario used (e.g., Figure 5.11a); in simulations with relatively weak wave forcing (resulting in a colder vortex than in the standard case), the excess moisture from Hunga makes less difference since ozone depletion is already severe under those conditions (Fleming et al., 2024). It should be noted that

those numerical modelling studies only perturbed water vapour, not stratospheric SO_2 or aerosols. In contrast, simulations with three CCMs conducted as part of HTHH-MOC included the effects of both the water vapour and aerosol perturbations from Hunga, each in isolation as well as the two in combination to assess their relative contributions. In these three models, the Hunga-induced impact on the 2023 Antarctic ozone hole ranged from statistically non-significant reductions of less than 10 DU to significant reductions of as much as 50 DU, with about half the decrease due to chemical destruction (Figure 5.12, Figure S3.41; see also Figures S3.42 and S3.43 for the simulated post-Hunga halogen repartitioning in the SH lower stratosphere; Bednarz et al., 2025). The Hunga SO_2 injection and subsequent aerosol formation, rather than the H_2O injection, was determined to be the primary driver of the additional chemical ozone loss (Figure 5.12; Figures S3.41- S3.43). Given the relatively weak forced response to the eruption, multi-member ensembles should be performed by each model to ensure robust diagnosis (Bednarz et al., 2025), and further multi-model evaluation should aim to reduce the spread in results. Across most modelling studies, the additional total column ozone loss in the polar vortex attributed to Hunga was within typical climatological variability and thus may not be readily detectable in the current observational record.

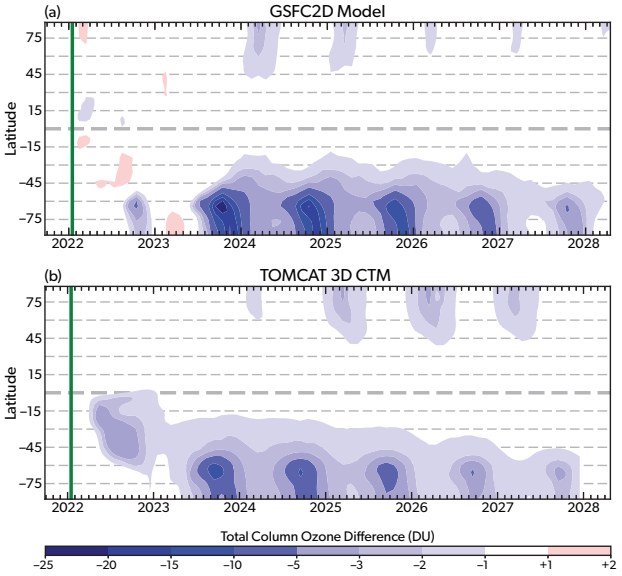

Figure 5.11: *Calculated impact over 2022–2028 of the Hunga eruption on total column ozone, quantified by taking differences between simulations with and without inclusion of the Hunga injection of H_2O. Total ozone differences (in DU) are shown from (a) a 2-D model (GSFC2D), adapted from Fleming et al. (2024), and (b) a 3-D CTM (TOMCAT), adapted from Zhou et al. (2024). The vertical green line marks the date of the Hunga eruption.*

Antarctic winter/spring of 2024 The Antarctic vortex was unusually dynamically disturbed in 2024, with two consecutive sudden stratospheric warming (SSW) events occurring in July and August (Zi et al., 2025). Unusually large values of the maximum gradient in scaled potential vorticity are consistent with increased wave activity (Figures 5.8b,j,r; Santee et al., 2024). Consequently, temperatures were near or above average through most of the season (Figures 5.8c,k,s). Water vapour remained exceptionally high, especially at 750 K (Figure 5.8d), where mixing ratios were initially about 1–2 ppmv higher than those observed in 2023, consistent with continued slow transport in the BDC bringing the Hunga hydration to the southern polar middle stratosphere (Millán et al., 2024). In the lower stratosphere (Figures 5.8l,t), the anomalously moist conditions at the start of May again led to greater-than-average dehydration during the winter, albeit to a lesser degree than in 2023. Such year-to-year reduction in the magnitude of Hunga-enhanced Antarctic dehydration is in line with expectations (Millán et al., 2024; Zhou et al., 2024) and is also consistent with the generally slightly higher temperatures in 2024. The evolution of HNO_3 (Figures 5.8e,m,u) was mostly within its climatological range, suggesting that the denitrification process was not substantially perturbed. The chlorine species also more or less followed typical seasonal patterns in the lower stratosphere. At 750 K, however, anomalous chlorine activation, with unprecedented low HCl and a spike in ClO (Figures 5.8f,g), was observed in mid-August during a period of strong wave activity (Figure 5.8b; Zi et al., 2025). Although the highly perturbed vortex shrank considerably at this time (Figure 5.8a), it was elongated and shifted off the pole (not shown), enabling greater exposure to sunlight and thus atypically large vortex-averaged ClO values. The SSW event also transported ozone poleward, causing vortex-averaged ozone to be marginally above the previously observed range at this level in mid-August (Figure 5.8h). Consistent with the unremarkable progression of chlorine activation in the lower stratosphere, ozone abundances there were near or slightly above average through most of the season (Figures 5.8p,x). Common metrics of Antarctic springtime ozone (e.g., September ozone hole area, ozone mass deficit, and polar-cap-averaged

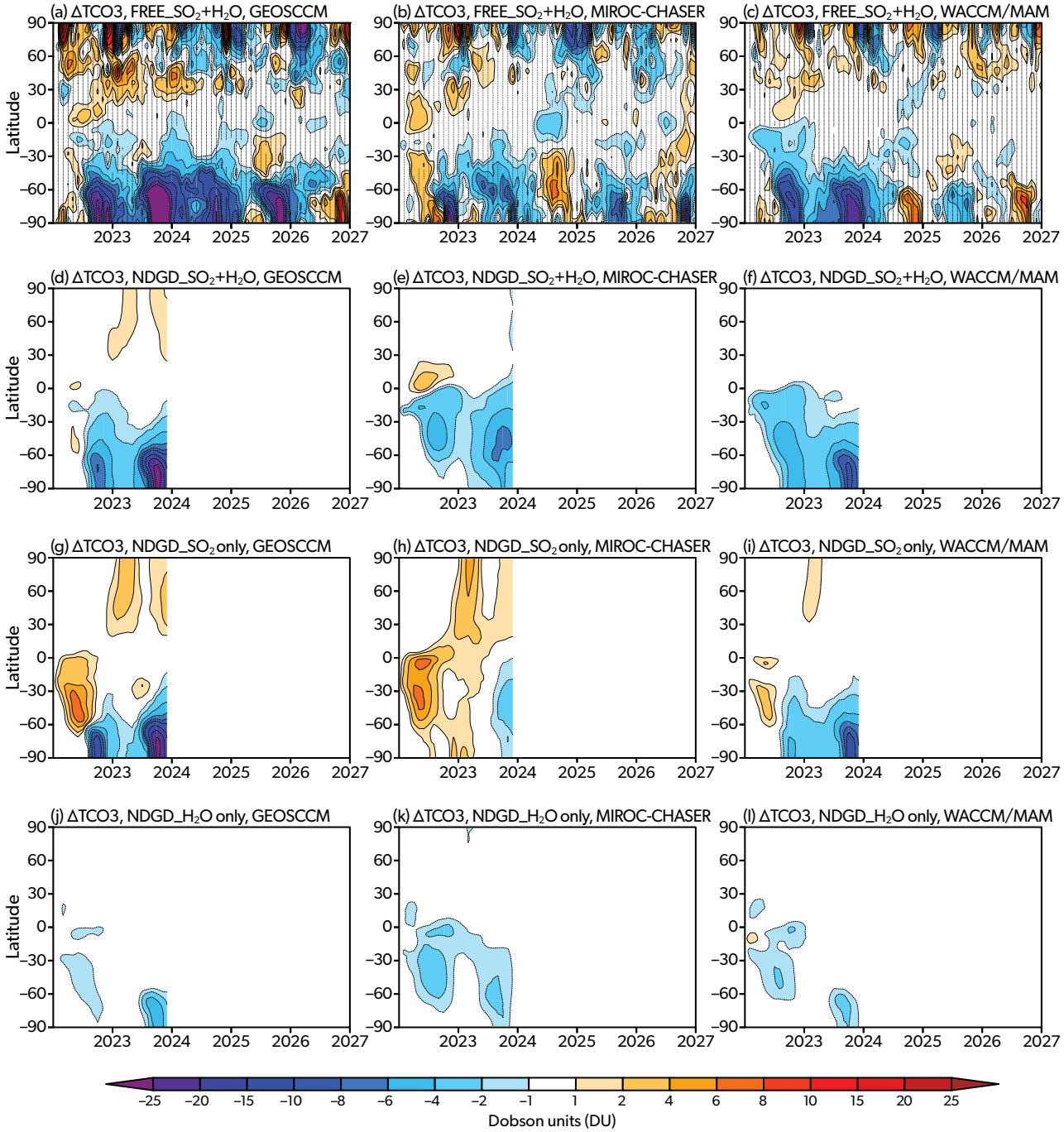

Figure 5.12: *Hunga-induced changes in total column ozone, calculated as the differences (perturbed minus control) between simulations with and without Hunga forcing. Results are from the NASA GEOSCCM (a,d,g,j), the MIROC-CHASER version 6 (b,e,h,k), and WACCM6 coupled to the MAM module version 4 (c,f,i,l). In all cases the ensemble-mean response is shown. (a–c) Results from free-running experiments including injection of both 0.5 Tg of SO_2 and ~150 Tg of H_2O from Hunga (FREE_SO_2+H_2O). Stippling marks regions where the response in total ozone is not statistically significant. (d–f) Results from specified-dynamics experiments driven by atmospheric winds and temperatures from MERRA-2 and including injection of both SO_2 and H_2O (NDGD_SO_2+H_2O). Since the meteorology is identical for the perturbed and control runs, these experiments quantify the direct chemical effects of the eruption on ozone and do not reflect those arising from changes in temperature or circulation. (g–i) Results from specified-dynamics experiments in which only SO_2 is injected (NDGD_SO_2only). (j–l) Results from specified-dynamics experiments in which only H_2O is injected (NDGD_H_2Oonly). The bottom two rows allow the effects of the aerosol and water-vapour perturbations from Hunga to be isolated. From Bednarz et al. (2025).*

column ozone) similarly show values well within the climatological range (Wargan et al., 2025).

5.3.4 Arctic winters/springs of 2021/2022, 2022/2023, and 2023/2024

The 2021/2022 polar vortex was colder than usual, especially between late January and March 2022, when minimum temperatures in the lower stratosphere were about one standard deviation below the climatological mean (Figure 5.13a; Bernhard et al., 2023). While the 2022/2023 Arctic winter started with temperatures below the long-term average in January 2023 (Figure 5.13a), a major SSW on 16 February 2023 caused the vortex to break up by the end of February, before chlorine-catalysed ozone loss could have a major effect (Druckenmiller et al., 2024). The 2023/2024 Arctic vortex was weaker, warmer, and more dynamically active than typical (Newman et al., 2024). Although the vortex recovered from an early major SSW on 16 January 2024, a second major SSW on 4 March caused the early breakup of the vortex (Figure 5.13a; Lee et al., 2024). Conditions during the 2022/2023 and 2023/2024 seasons were unfavourable for ozone loss catalysed by heterogeneous reactions, precluding a significant effect from the Hunga eruption on ozone depletion in these years. Whether the generally warm and disturbed conditions in these years were, at least partly, a consequence of dynamical changes induced by the eruption remains an open question. In a first study, results from the SOCOLv4 CCM suggest that the increased water vapour from Hunga reduced the temperature gradient between the tropics and the polar regions, weakening the Arctic stratospheric polar vortex in 2022/2023 and possibly causing conditions conducive to an SSW event (Kuchar et al., 2025). Ongoing analysis of HTHH-MOC simulations may shed further light on this issue.

We now turn to the evolution of water vapour, ozone, and related constituents in the years following the eruption. In spring 2022, the increased water vapour from Hunga had not yet reached the northern polar latitudes (Chapter 3, Figure 3.8), while in the winter/spring season of 2022/2023, it was not able to penetrate the polar vortex (Druckenmiller et al., 2024). Thus, through most of the late winter/spring in both 2021/2022 and 2022/2023, water vapour mixing ratios were close to the long-term mean (Figure 5.13b). Consistent with the meteorological conditions, the minimum daily total column ozone observed in March 2022 in the polar vortex was slightly lower than the climatological mean (Bernhard et al., 2023), whereas in spring 2023 it was slightly higher (Druckenmiller et al., 2024).

In contrast to the prior two years, increased water vapour values were observed by MLS inside the 2023/2024 Arctic vortex (Figure 5.13b). The 2023/2024 season also showed relatively high ClO abundances (Figure 5.13e) and corresponding low HCl abundances (Figure 5.13d) at 500 K (~42 hPa, ~21 km) compared to the long-term mean in December and January, consistent with an increased probability of PSCs induced by the increased water vapour. In addition, vortex minimum temperatures at that level were below average from late November to late December 2023, and the vortex shifted off the pole into sunlit regions, enabling strong ClO enhancement; ClO abundances then declined after mid-January 2024 as the temperatures rose and the vortex moved back over the pole (Figure 5.13a,e; Lee et al., 2024). Ozone values at 500 K were observed to be below average in late December 2023/January 2024, but they returned to near or above average in February (Figure 5.13f), consistent with the variations in chlorine activation. Chemical changes in vortex-averaged ozone can arise from variations in PSC occurrence induced by both temperature fluctuations and changes in water vapour. Furthermore, it is important to emphasise that ozone is controlled by both chemical and dynamical effects. Indeed, over the 2023/2024 winter/spring, a series of planetary-scale wave events propagating upward from the troposphere forced poleward and downward advection of ozone into the lower stratosphere, resulting in record-high Arctic polar-cap total column ozone amounts in March 2024 (Figure 5.1; Newman et al., 2024). Note, however, that the caution stated earlier (in the description of the 2022 Antarctic winter in Section 5.3.3)—that polar-cap averages and vortex averages encompass very different regions and thus are not directly comparable—is even more applicable in the Arctic, where the vortex is typically elongated, shifted off the pole, and tilted with altitude. Quantification of chemical ozone loss in the Arctic requires a detailed accounting of transport effects; such studies have not yet been conducted for any of the post-Hunga Arctic winters.

The increase of Arctic ozone loss through the combined effects of the Hunga water vapour and temperature perturbations projected by the GSFC2D model is small (4–5 DU) and does not start until spring 2024 (Figure 5.11a; Fleming et al., 2024). The model is not constrained by observed meteorological conditions, but rather uses constant tropospheric planetary-wave

driving for the lower boundary conditions, based on a 30-year (1991–2020) average of MERRA-2 data. Sensitivity calculations with the strength of the wave driving varied to mimic the interannual range of observed stratospheric temperatures show that the Hunga water vapour and temperature perturbations have only a small effect on the expected interannual range of ozone loss (Fleming et al., 2024). Similarly, HTHH-MOC simulations including the effects of both the water vapour and the aerosol perturbations show no statistically significant changes in Arctic total column ozone in any post-Hunga winter (Figure 5.12; Bednarz et al., 2025).

5.4 Predictions of the future impacts on the stratospheric ozone layer

Predictions based on current observations and model simulations indicate that the Hunga hydration will persist for some time, with removal occurring on a timescale of several years to a decade. Accordingly, the effects on ozone and other trace gases discussed in Section 5.3 for 2022–2024 can be expected to continue over the coming years, albeit to a decreasing extent as the excess water vapour is slowly removed. This section discusses observational and global modelling studies that have examined these effects. At the time of publication, work on HTHH-MOC experiments is ongoing. We expect that these and other model studies will further elucidate the possible impacts from the Hunga eruption on stratospheric chemistry and composition in the future.

5.4.1 Future evolution of stratospheric water vapour

It took ~1–1.5 years for the water vapour injected into the stratosphere by the eruption to be distributed globally (see Chapters 3 and 4; Millán et al., 2024; Zhou et al., 2024). The stratosphere is dehydrated primarily by stratosphere-to-troposphere transport (STT) at middle and high latitudes as part of the meridional Brewer–Dobson circulation and by sedimentation of ice PSCs in the Antarctic vortex (dehydration); photodissociation in the mesosphere also plays a small role (see discussion in Millán et al., 2024). Measurements and model simulations identify dehydration in Antarctic winter as the primary removal pathway at work initially (Millán et al., 2024; Zhou et al., 2024). Because the Hunga water vapour was effectively excluded from the 2022 Antarctic vortex (see Section 5.3.3), removal did not begin until dehydration in the 2023 austral winter. Removal through STT did not come into play until the Hunga-hydrated air parcels had descended to sufficiently low altitudes (below ~16 km, ~100 hPa, ~380 K), but loss via STT started to exceed that from Antarctic dehydration in late 2023 (Zhou et al., 2025). Both removal processes (STT and dehydration through ice PSC sedimentation) will continue over the coming years. Estimates based on observations and model simulations of the e-folding timescale for the decay of the excess Hunga water vapour once removal commenced range between 2.5 and 4 years (Fleming et al., 2024; Khaykin et al., 2022; Kuchar et al., 2025; Schoeberl et al., 2025; Zhou et al., 2024; Zhou et al., 2025; Zhuo et al., 2025). Accounting for the ~1.5-year lag time before removal processes began, the lifetime (i.e., mean stratospheric residence time) of the Hunga water vapour is estimated to be about 4–5.5 years (Schoeberl et al., 2025).

5.4.2 Future Hunga-related changes in stratospheric composition

The long-term impact of Hunga water vapour on ozone and related gases is clearly controlled by the timescale of the removal of the additional water vapour (Section 5.4.1). The decreasing chemical impacts will also extend over this same timescale of the next decade or so.

Global model studies indicate that the largest impact of Hunga on column ozone will occur in the polar regions, particularly the Antarctic. Transport of the Hunga cloud to the Arctic took longer (see Chapters 3 and 4), by which time the magnitude of the additional water vapour had decreased through global mixing. Moreover, the occurrence of cold conditions leading to substantial ozone depletion exhibits strong interannual variability. Figure 5.11 shows the predicted effect of the Hunga water vapour alone on column ozone from simulations using the GSFC2D 2-D model (Fleming et al., 2024) and the TOMCAT 3-D CTM (Zhou et al., 2024). It should be noted that neither of these studies considered the effects of enhanced stratospheric aerosol following the eruption. Both models show the largest column impact of the excess water vapour in the Antarctic from 2023 onwards, although the modelled impact is substantially larger in GSFC2D (Figure 5.11a) than in TOMCAT (Figure 5.11b). Note that the GSFC2D simulation shown in the figure uses standard wave driving, which gives an additional depletion of 20 DU, at the high end of the 13–23 DU range for different forcings discussed in the description of the 2023 Antarctic winter in Section 5.3.3. However, aside from the difference in absolute impact,

the qualitative behaviour of a decreasing effect in the SH is similar in both models, particularly from 2024 onwards. In the NH, the GSFC2D model produces the largest impact in 2024, whereas in TOMCAT, which has slower transport to the Arctic, the effect is largest in 2026. HTHH-MOC CCM simulations, in which both the water vapour and the aerosol perturbations from Hunga are considered, similarly show that the largest impacts on column ozone occur in the Antarctic and generally diminish after 2024, with the timing of the strongest effects in the Arctic varying between the different models (Figure 5.12; Bednarz et al., 2025). The modelled effects of Hunga on ozone persist until approximately 2030, although they become relatively small as the excess water vapour is removed from the stratosphere (Figure 5.11). Observations obtained by late 2024 suggest that additional chemical depletion attributable to Hunga in the Antarctic in 2023 and 2024 was small (see Section 5.3.3), so the impact may be overestimated in the models.

The impact of the Hunga H_2O anomaly on total ozone is generally less than ~10% (Figures 5.11 and 5.12), smaller than the year-to-year variability characteristic of the stratospheric polar regions during winter and spring. The standard deviation of the observed SH October–November polar-cap total ozone (~35 DU during 1991–2022; Fleming et al., 2024) exceeds most of the maximum model-estimated changes. Therefore, the fingerprint of the response to the Hunga eruption may not be easily detectable above the background variability in the current record of total ozone observations. However, the transient suppression of ozone abundances by the additional water vapour and aerosol may affect the estimation of long-term trends during the Hunga period and complicate detection of the signal of ozone recovery.

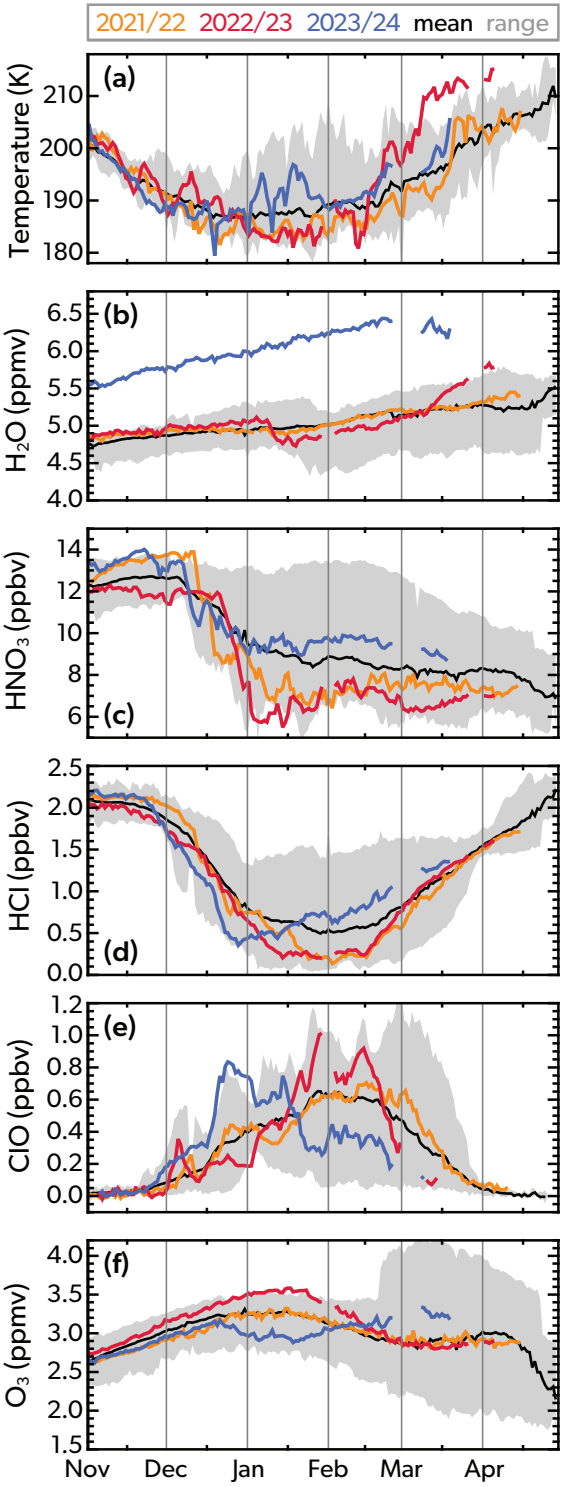

Figure 5.13: *Evolution from November through April of daily MLS (a) minimum temperature inside the Arctic polar vortex, and (b) H_2O, (c) HNO_3, (d) HCl, (e) daytime-only ClO, and (f) O_3, averaged within the vortex at 500 K (~42 hPa, ~21 km) for selected winters/springs: 2021/2022 (orange), 2022/2023 (red), and 2023/2024 (blue). Grey shading marks the range of values and the black line the climatological mean over 2005–2021.*

References

Aquila, V., L. D. Oman, R. Stolarski, A. R. Douglass and P. A. Newman (2013). 'The Response of Ozone and Nitrogen Dioxide to the Eruption of Mt. Pinatubo at Southern and Northern Midlatitudes'. *J. Atmos. Sci.*, 70, pp. 894–900. DOI: 10.1175/jas-d-12-0143.1.

Bednarz, E. M., V. Aquila, A. H. Butler, P. Colarco, E. Fleming, F. F. Østerstrøm, D. Plummer, I. Quaglia, W. Randel, M. L. Santee et al. (2025). 'Multi-model assessment of impacts of the 2022 Hunga eruption on stratospheric ozone and its chemical and dynamical drivers'. *EGUsphere [preprint]*, 2025, pp. 1–24. DOI: 10.5194/egusphere-2025-4609.

Bernhard, G. H., V. E. Fioletov, J.-U. Grooß, I. Ialongo, B. Johnson, K. Lakkala, G. L. Manney, R. Müller and T. Svendby (2023). 'Ozone and UV radiation [in "State of the Climate in 2022"]'. *Bull. Amer. Meteor. Soc.*, 104, S308–S310. DOI: 10.1175/BAMS-D-23-0079.1.

DeLand, M. T. and M. R. Schoeberl (2025). 'Polar Stratospheric Cloud Observations From the OMPS Limb Profiler'. *J. Geophys. Res.*, 130, e2024JD042632. DOI: 10.1029/2024jd042632.

Deshler, T., L. E. Kalnajs, M. Norgren, Y. Zhu and J. Zhang (2024). 'In Situ Aerosol Size Spectra Measurements in the Austral Polar Vortex Before and After the Hunga Tonga-Hunga Ha'apai Volcanic Eruption'. *Geophys. Res. Lett.*, 51, e2024GL111388. DOI: 10.1029/2024gl111388.

Druckenmiller, M. L., R. L. Thoman, T. A. Moon, L. M. Andreassen, T. J. Ballinger, L. T. Berner, G. H. Bernhard, U. S. Bhatt, S. Bigalke, J. W. Bjerke et al. (2024). 'The Arctic'. *Bull. Am. Meteorol. Soc.*, 105, S277–S330. DOI: 10.1175/bams-d-24-0101.1.

Evan, S., J. Brioude, K. H. Rosenlof, R.-S. Gao, R. W. Portmann, Y. Zhu, R. Volkamer, C. F. Lee, J.-M. Metzger, K. Lamy et al. (2023). 'Rapid ozone depletion after humidification of the stratosphere by the Hunga Tonga eruption'. *Science*, 382, eadg2551. DOI: 10.1126/science.adg2551.

Fahey, D. W., S. R. Kawa, E. L. Woodbridge, P. Tin, J. C. Wilson, H. H. Jonsson, J. E. Dye, D. Baumgardner, S. Borrmann, D. W. Toohey et al. (1993). 'In situ measurements constraining the role of sulphate aerosols in mid-latitude ozone depletion'. *Nature*, 363, pp. 509–514. DOI: 10.1038/363509a0.

Fleming, E. L., P. A. Newman, Q. Liang and L. D. Oman (2024). 'Stratospheric Temperature and Ozone Impacts of the Hunga Tonga-Hunga Ha'apai Water Vapor Injection'. *J. Geophys. Res.*, 129, e2023JD039298. DOI: 10.1029/2023jd039298.

Frith, S. M., N. A. Kramarova, R. S. Stolarski, R. D. McPeters, P. K. Bhartia and G. J. Labow (2014). 'Recent changes in total column ozone based on the SBUV Version 8.6 Merged Ozone Data Set'. *J. Geophys. Res.*, 119, pp. 9735–9751. DOI: 10.1002/2014jd021889.

Frith, S. M., R. S. Stolarski, N. A. Kramarova and R. D. McPeters (2017). 'Estimating uncertainties in the SBUV Version 8.6 merged profile ozone data set'. *Atmos. Chem. Phys.*, 17, pp. 14695–14707. DOI: 10.5194/acp-17-14695-2017.

Godin-Beekmann, S., N. Azouz, V. F. Sofieva, D. Hubert, I. Petropavlovskikh, P. Effertz, G. Ancellet, D. A. Degenstein, D. Zawada, L. Froidevaux et al. (2022). 'Updated trends of the stratospheric ozone vertical distribution in the 60°S–60°N latitude range based on the LOTUS regression model'. *Atmos. Chem. Phys.*, 22, pp. 11657–11673. DOI: 10.5194/acp-22-11657-2022.

Junge, C. E., C. W. Chagnon and J. E. Manson (1961). 'Stratospheric aerosols'. *J. Atmos. Sci.*, 18, pp. 81–108. DOI: 10.1175/1520-0469(1961)018<0081:sa>2.0.co;2.

Khaykin, S., A. Podglajen, F. Ploeger, J.-U. Grooß, F. Tence, S. Bekki, K. Khlopenkov, K. Bedka, L. Rieger, A. Baron et al. (2022). 'Global perturbation of stratospheric water and aerosol burden by Hunga eruption'. *Commun. Earth Environ.*, 3, 316. DOI: 10.1038/s43247-022-00652-x.

Kinnison, D. E., K. E. Grant, P. S. Connell, D. A. Rotman and D. J. Wuebbles (1994). 'The chemical and radiative effects of the Mount Pinatubo eruption'. *J. Geophys. Res.*, 99, pp. 25705–25731. DOI: 10.1029/94jd02318.

Kramarova, N. A., P. A. Newman, L. R. Lait, B. Johnson, M. Pitts, M. L. Santee, I. Petropavlovskikh, L. Coy and J. De Laat (2024). '2023 Antarctic ozone hole [in "State of the Climate in 2023"]'. *Bull. Amer. Meteor. Soc.*, 105, S358–S361. DOI: 10.1175/BAMS-D-24-0099.1.

Kuchar, A., T. Sukhodolov, G. Chiodo, A. Jörimann, J. Kult-Herdin, E. Rozanov and H. H. Rieder (2025). 'Modulation of the northern polar vortex by the Hunga Tonga–Hunga Ha'apai eruption and the associated surface response'. *Atmos. Chem. Phys.*, 25, pp. 3623–3634. DOI: 10.5194/acp-25-3623-2025.

Lawrence, Z. D., G. L. Manney and K. Wargan (2018). 'Reanalysis intercomparisons of stratospheric polar processing diagnostics'. *Atmos. Chem. Phys.*, 18,

pp. 13547–13579. DOI: 10.5194/acp-18-13547-2018.

Lecours, M., C. D. Boone and P. F. Bernath (2024). 'Antarctic Polar Stratospheric Cloud Analysis of ACE-FTS Data From 2005 to 2023'. *J. Geophys. Res.*, 129, e2024JD040990. DOI: 10.1029/2024jd040990.

Lee, S. H., A. H. Butler and G. L. Manney (2024). 'Two major sudden stratospheric warmings during winter 2023/2024'. *Weather*, 80, pp. 45–53. DOI: 10.1002/wea.7656.

Manney, G. L., M. L. Santee, A. Lambert, L. F. Millán, K. Minschwaner, F. Werner, Z. D. Lawrence, W. G. Read, N. J. Livesey and T. Wang (2023). 'Siege in the Southern Stratosphere: Hunga Tonga-Hunga Ha'apai Water Vapor Excluded From the 2022 Antarctic Polar Vortex'. *Geophys. Res. Lett.*, 50. DOI: 10.1029/2023gl103855.

Millán, L., W. G. Read, M. L. Santee, A. Lambert, G. L. Manney, J. L. Neu, M. C. Pitts, F. Werner, N. J. Livesey and M. J. Schwartz (2024). 'The Evolution of the Hunga Hydration in a Moistening Stratosphere'. *Geophys. Res. Lett.*, 51, e2024GL110841. DOI: 10.1029/2024gl110841.

Millán, L., M. L. Santee, A. Lambert, N. J. Livesey, F. Werner, M. J. Schwartz, H. C. Pumphrey, G. L. Manney, Y. Wang, H. Su et al. (2022). 'The Hunga Tonga-Hunga Ha'apai Hydration of the Stratosphere'. *Geophys. Res. Lett.*, 49, e2022GL099381. DOI: 10.1029/2022gl099381.

Nedoluha, G. E., R. M. Gomez, I. Boyd, H. Neal, D. R. Allen, A. Parrish, B. J. Connor and D. E. Siskind (2025). 'Measurements of Stratospheric ClO From Mauna Kea: 1992–2023'. *J. Geophys. Res.*, 130, e2024JD041848. DOI: 10.1029/2024jd041848.

Newman, P. A., L. R. Lait, N. A. Kramarova, L. Coy, S. M. Frith, L. D. Oman and S. S. Dhomse (2024). 'Record High March 2024 Arctic Total Column Ozone'. *Geophys. Res. Lett.*, 51, e2024GL110924. DOI: 10.1029/2024gl110924.

Santee, M. L., A. Lambert, L. Froidevaux, G. L. Manney, M. J. Schwartz, L. F. Millán, N. J. Livesey, W. G. Read, F. Werner and R. A. Fuller (2023). 'Strong Evidence of Heterogeneous Processing on Stratospheric Sulfate Aerosol in the Extrapolar Southern Hemisphere Following the 2022 Hunga Tonga-Hunga Ha'apai Eruption'. *J. Geophys. Res.*, 128, e2023JD039169. DOI: 10.1029/2023jd039169.

Santee, M. L., A. Lambert, G. L. Manney, N. J. Livesey, L. Froidevaux, J. L. Neu, M. J. Schwartz, L. F. Millán, F. Werner, W. G. Read et al. (2022). 'Prolonged and Pervasive Perturbations in the Composition of the Southern Hemisphere Midlatitude Lower Stratosphere From the Australian New Year's Fires'. *Geophys. Res. Lett.*, 49, e2021GL096270. DOI: 10.1029/2021gl096270.

Santee, M. L., G. L. Manney, A. Lambert, L. F. Millán, N. J. Livesey, M. C. Pitts, L. Froidevaux, W. G. Read and R. A. Fuller (2024). 'The Influence of Stratospheric Hydration From the Hunga Eruption on Chemical Processing in the 2023 Antarctic Vortex'. *J. Geophys. Res.*, 129, e2023JD040687. DOI: 10.1029/2023jd040687.

Schoeberl, M. R., M. Toohey, Y. Wang and R. Ueyama (2025). 'Stratospheric Injection Lifetimes'. *J. Geophys. Res.*, 130, e2025JD043928. DOI: 10.1029/2025jd043928.

Schoeberl, M. R., Y. Wang, R. Ueyama, G. Taha, E. Jensen and W. Yu (2022). 'Analysis and Impact of the Hunga Tonga-Hunga Ha'apai Stratospheric Water Vapor Plume'. *Geophys. Res. Lett.*, 49, e2022GL100248. DOI: 10.1029/2022gl100248.

Smale, D., M. P. Chipperfield, R. Querel, G. E. Nedoluha, U. Frieß, J. Robinson, S. Nichol, S. Heddell, W. Feng, R. M. Gomez et al. (2025). 'The impact of the Hunga Tonga-Hunga Ha'apai volcanic eruption on the 2023 Antarctic Ozone hole, as observed from Arrival Heights, Antarctica'. *J. Atmos. Chem.*, 82. DOI: 10.1007/s10874-025-09478-1.

Solomon, S. (1999). 'Stratospheric ozone depletion: A review of concepts and history'. *Rev. Geophys.*, 37, pp. 275–316. DOI: 10.1029/1999rg900008.

Solomon, S., K. Stone, P. Yu, D. M. Murphy, D. Kinnison, A. R. Ravishankara and P. Wang (2023). 'Chlorine activation and enhanced ozone depletion induced by wildfire aerosol'. *Nature*, 615, pp. 259–264. DOI: 10.1038/s41586-022-05683-0.

Strahan, S. E., D. Smale, S. Solomon, G. Taha, M. R. Damon, S. D. Steenrod, N. Jones, B. Liley, R. Querel and J. Robinson (2022). 'Unexpected repartitioning of stratospheric inorganic chlorine after the 2020 Australian wildfires'. *Geophys. Res. Lett.*, 49, e2022GL098290. DOI: 10.1029/2022GL098290.

Taha, G., R. Loughman, P. R. Colarco, T. Zhu, L. W. Thomason and G. Jaross (2022). 'Tracking the 2022 Hunga Tonga-Hunga Ha'apai Aerosol Cloud in the Upper and Middle Stratosphere Using Space-Based Observations'. *Geophys. Res. Lett.*, 49, e2022GL100091. DOI: 10.1029/2022gl100091.

Tritscher, I., M. C. Pitts, L. R. Poole, S. P. Alexander, F. Cairo, M. P. Chipperfield, J.-U. Grooß, M. Höpfner, A. Lambert, B. Luo et al. (2021). 'Polar Stratospheric Clouds: Satellite Observations, Processes,

and Role in Ozone Depletion'. *Rev. Geophys.*, 59, e2020RG000702. DOI: 10.1029/2020rg000702.

Van Eaton, A. R., J. Lapierre, S. A. Behnke, C. Vagasky, C. J. Schultz, M. Pavolonis, K. Bedka and K. Khlopenkov (2023). 'Lightning Rings and Gravity Waves: Insights Into the Giant Eruption Plume From Tonga's Hunga Volcano on 15 January 2022'. *Geophys. Res. Lett.*, 50, e2022GL102341. DOI: 10.1029/2022gl102341.

Wang, X., W. Randel, Y. Zhu, S. Tilmes, J. Starr, W. Yu, R. Garcia, O. B. Toon, M. Park, D. Kinnison et al. (2023). 'Stratospheric Climate Anomalies and Ozone Loss Caused by the Hunga Tonga-Hunga Ha'apai Volcanic Eruption'. *J. Geophys. Res.*, 128, e2023JD039480. DOI: 10.1029/2023jd039480.

Wargan, K., G. L. Manney and N. J. Livesey (2025). 'Factors Contributing to the Unusually Low Antarctic Springtime Ozone in 2020–2023'. *J. Geophys. Res.*, 130, e2025JD043621. DOI: 10.1029/2025jd043621.

Weber, M., W. Steinbrecht, C. Arosio, R. van der A, S. Frith, J. Anderson, L. Ciasto, M. Coldewey-Egbers, S. Davis, D. Degenstein et al. (2024). 'Stratospheric ozone [in "State of the Climate in 2023"]'. *Bull. Amer. Meteor. Soc.*, 105, S99–S100. DOI: 10.1175/BAMS-D-24-0116.1.

Wilmouth, D. M., F. F. Østerstrøm, J. B. Smith, J. G. Anderson and R. J. Salawitch (2023). 'Impact of the Hunga Tonga volcanic eruption on stratospheric composition'. *Proc. Natl. Acad. Sci.*, 120, e2301994120. DOI: 10.1073/pnas.2301994120.

Wohltmann, I., M. L. Santee, G. L. Manney and L. F. Millán (2024). 'The Chemical Effect of Increased Water Vapor From the Hunga Tonga-Hunga Ha'apai Eruption on the Antarctic Ozone Hole'. *Geophys. Res. Lett.*, 51, e2023GL106980. DOI: 10.1029/2023gl106980.

World Meteorological Organization (WMO) (2022). *Scientific Assessment of Ozone Depletion: 2022*. Tech. rep. GAW Report No. 278. Geneva, Switzerland.

Zhang, J., D. Kinnison, Y. Zhu, X. Wang, S. Tilmes, K. Dube and W. Randel (2024a). 'Chemistry Contribution to Stratospheric Ozone Depletion After the Unprecedented Water-Rich Hunga Tonga Eruption'. *Geophys. Res. Lett.*, 51, e2023GL105762. DOI: 10.1029/2023gl105762.

Zhang, J., P. Wang, D. Kinnison, S. Solomon, J. Guan, K. Stone and Y. Zhu (2024b). 'Stratospheric Chlorine Processing After the Unprecedented Hunga Tonga Eruption'. *Geophys. Res. Lett.*, 51, e2024GL108649. DOI: 10.1029/2024gl108649.

Zhou, X., Q. Chen, W. Feng, S. Heddell, S. S. Dhomse, G. Mann, H. C. Pumphrey, L. Millán, M. L. Santee and M. P. Chipperfield (2025). 'When will the stratospheric water vapour return to pre-Hunga level?' *Commun. Earth Environ.*, submitted, manuscript COMMSENV-25-4119-T.

Zhou, X., S. S. Dhomse, W. Feng, G. Mann, S. Heddell, H. Pumphrey, B. J. Kerridge, B. Latter, R. Siddans, L. Ventress et al. (2024). 'Antarctic Vortex Dehydration in 2023 as a Substantial Removal Pathway for Hunga Tonga-Hunga Ha'apai Water Vapor'. *Geophys. Res. Lett.*, 51, e2023GL107630. DOI: 10.1029/2023gl107630.

Zhu, Y., C. G. Bardeen, S. Tilmes, M. J. Mills, X. Wang, V. L. Harvey, G. Taha, D. Kinnison, R. W. Portmann, P. Yu et al. (2022). 'Perturbations in stratospheric aerosol evolution due to the water-rich plume of the 2022 Hunga-Tonga eruption'. *Commun. Earth Environ.*, 3, 248. DOI: 10.1038/s43247-022-00580-w.

Zhu, Y., R. W. Portmann, D. Kinnison, O. B. Toon, L. Millán, J. Zhang, H. Vömel, S. Tilmes, C. G. Bardeen, X. Wang et al. (2023). 'Stratospheric ozone depletion inside the volcanic plume shortly after the 2022 Hunga Tonga eruption'. *Atmos. Chem. Phys.*, 23, pp. 13355–13367. DOI: 10.5194/acp-23-13355-2023.

Zhuo, Z., X. Wang, Y. Zhu, W. Yu, E. M. Bednarz, E. Fleming, P. R. Colarco, S. Watanabe, D. Plummer, G. Stenchikov et al. (2025). 'Comparing multimodel ensemble simulations with observations and decadal projections of upper atmospheric variations following the Hunga eruption'. *Atmos. Chem. Phys.*, 25, pp. 13161–13176. DOI: 10.5194/acp-25-13161-2025.

Zi, Y., Z. Long, J. Sheng, G. Lu, W. Perrie and Z. Xiao (2025). 'The Sudden Stratospheric Warming Events in the Antarctic in 2024'. *Geophys. Res. Lett.*, 52, e2025GL115257. DOI: 10.1029/2025gl115257.